geosciences

MDPI

Article

Provenance and Tectonic Evolution of Lower Ediacaran Siliciclastics Along the Northern Gondwana Margin: Geochemical and Isotopic Evidence from the Saghro Group (Anti-Atlas, Morocco)

Mohamed Hamouyahia [1,2,*], Nasrrddine Youbi [1,3,4], Brian Cousens [5], Abderrahmane Soulaimani [1], Hassane Oubaassine [1,6], Hicheme Houane [1,2], Youssef Atif [7], El Hassane Chellai [1], Moulay Ahmed Boumehdi [1,3], Lhou Maacha [2], Mohamed Zouhair [2] and Lahcen Rakhiss [2]

1 Department of Geology, Faculty of Sciences-Semlalia, Cadi Ayyad University, Prince Moulay Abdellah Boulevard, Marrakech 40000, Morocco; youbi@uca.ac.ma (N.Y.); soulaimani@uca.ac.ma (A.S.); hassane.oubaassine@ced.uca.ma (H.O.); h.houane.ced@uca.ac.ma (H.H.); chell@uca.ac.ma (E.H.C.); boumehdi@uca.ac.ma (M.A.B.)
2 Managem Group, Twin Center, Tour A, Angle 191, Bd Mohamed Zerktouni, Casablanca 20100, Morocco; l.maacha@managemgroup.com (L.M.); m.zouhair@managemgroup.com (M.Z.); l.rakhiss@managemgroup.com (L.R.)
3 Instituto Dom Luiz, Faculdade de Ciências, Universidade de Lisboa, 1749-016 Lisboa, Portugal
4 Faculty of Geology and Geography, Tomsk State University, 36 Lenin Ave, Tomsk 634050, Russia
5 Department of Earth and Sciences, Carleton University, Ottawa, ON K1S 5B6, Canada; briancousens@cunet.carleton.ca
6 Ministry for Energy Transition and Sustainable Development. N°9, Al Araar Avenue, 420/1 Secteur 16, Hay Riad, Rabat 10100, Morocco
7 Laboratory of Geosciences, Environment and Related Resources (GERA), Department of Geology, Faculty of Sciences Dhar El Mahraz, Sidi Mohamed Ben Abdellah University, Fez 30000, Morocco; youssef.atif@usmba.ac.ma
* Correspondence: m.hamouyahia.ced@uca.ac.ma

Abstract

This study investigates the provenance, weathering history, and tectono-sedimentary evolution of lower Ediacaran siliciclastic rocks of the Imiter Formation (Saghro Group, Imiter Sub-inlier, Anti-Atlas, Morocco) deposited along the northern margin of Gondwana. An integrated approach combining petrography, whole-rock major and trace element geochemistry, rare earth elements (REEs), Sm–Nd isotopes, and organic geochemistry (TOC and $\delta^{13}C_{org}$) was used to constrain sediment sources and depositional conditions. Geochemical proxies, including Th/Sc, La/Sc, and Zr/Sc ratios, together with REE distribution patterns, indicate that the sediments were mainly derived from felsic-to-intermediate rocks of the upper continental crust, with only minor sediment recycling. The negative εNd(t) values (−8.5 to −6.2) and Paleoproterozoic Nd model ages (1.6–2.1 Ga) further suggest the erosion of evolved crustal sources related to the West African Craton. Weathering indices (CIA, CIW, PIA) suggest weak-to-moderate chemical weathering under predominantly arid conditions. Redox-sensitive proxies (V–Ni, V/Cr, V/(V + Ni)) and low TOC content (0.1–0.3 wt.%) indicate deposition under mainly oxic-to-dysoxic conditions, with only transient reducing episodes. Tectonic discrimination diagrams, supported by regional magmatism, point to sedimentation within an extensional basin evolving from active-margin to continental rift conditions during the late Pan-African orogeny. The Imiter Formation records a system dominated by crustal recycling, syn-rift tectonics, and dynamic redox conditions in a shallow marine environment.

Check for updates

Academic Editor: Suzanne Golding

Received: 13 May 2026
Revised: 19 June 2026
Accepted: 24 June 2026
Published: 13 July 2026

Copyright: © 2026 by the authors. Licensee MDPI, Basel, Switzerland. This article is an open access article distributed under the terms and conditions of the Creative Commons Attribution (CC BY) license.

Keywords: Gondwana supercontinent; Anti-Atlas basement; Neoproterozoic; lower Ediacaran; Saghro Group; Geochemical proxies; Sm-Nd isotopes; total organic carbon (TOC); $\delta^{13}C_{org}$

1. Introduction

The geochemistry and isotopic composition of siliciclastic sedimentary rocks, particularly shales and sandstones, provide key constraints on sediment provenance, tectonic setting, and crustal evolution [1,2]. As products of weathering, erosion, and deposition, these rocks retain geochemical signatures reflecting both source lithology and surface processes [3,4]. Major, trace, and rare earth element (REE) systematics, together with their elemental ratios, are widely used to infer sediment provenance, paleoweathering intensity, and paleoclimatic conditions [5–10]. Ratios such as Th/Sc and La/Sc and REE fractionation patterns are particularly robust due to their relative immobility during weathering and diagenesis [1,2,11,12]. In addition, weathering indices such as the Chemical Index of Alteration (CIA), Plagioclase Index of Alteration (PIA), and Chemical Index of Weathering (CIW) are widely applied to quantify source-area alteration [13–15]. Complementarily, samarium–neodymium (Sm–Nd) isotopes provide reliable constraints on sediment provenance, with epsilon neodymium value at time t [εNd(t)] distinguishing juvenile from evolved crustal sources and Nd depleted-mantle model ages (T_{DM}) recording crustal residence times [16–18].

Shales are commonly regarded as representative proxies for the average composition of the upper continental crust, including Post-Archean Australian Shale (PAAS), upper continental crust (UCC), and North American Shale Composite (NASC) standards [3,19,20]. These deposits, therefore, constitute fundamental archives for reconstructing crustal composition and understanding sedimentary processes. In addition, because they form under variable climatic and redox conditions, they serve as valuable recorders of past environmental changes.

The Anti-Atlas belt in southern Morocco, located along the northern margin of the West African Craton (WAC), contains extensive Neoproterozoic sedimentary successions that record the evolution of sedimentary basins during this period. Among these units, the lower Ediacaran Saghro Group is particularly significant, although its depositional environment and exact age remain debated due to its structural complexity and the strong overprint of Pan-African tectonic events [21–25]. Within this group, the Imiter Formation is predominantly composed of siliciclastic rocks, chiefly shales and sandstones. The absence of fossils, however, makes the reconstruction of its depositional environment particularly challenging.

The Imiter Formation of the Saghro Group represents an important geological archive for investigating sediment provenance, weathering conditions, and basin evolution along the northern margin of the West African Craton (WAC). It records the interaction between crustal reworking, magmatic activity, and basin development during the late stages of the Pan-African orogeny [22,26,27]. In this context, shales record time-integrated crustal signals, whereas sandstones preserve more short-term source information, which makes the combined study of both lithologies especially valuable for provenance reconstruction.

This study presents new petrographic observations together with major and trace element data, total organic carbon (TOC), stable carbon isotopic compositions of organic carbon ($\delta^{13}C_{org}$), and Sm–Nd isotopic results from the lower Ediacaran Imiter Formation in the eastern Anti-Atlas of Morocco. The objectives are to (i) constrain sediment provenance and crustal evolution, (ii) determine the tectonic setting of basin development, (iii) assess

paleoweathering intensity in the source area, and (iv) reconstruct the paleoenvironmental and paleoredox conditions during deposition.

2. Geological Setting

2.1. The Anti-Atlas Belt

The Moroccan Anti-Atlas Mountains, located northwest of the West African Craton (WAC) (Figure 1a), represent a major segment of the Neoproterozoic orogenic belt surrounding the craton [28]. The belt is characterized by WSW–ENE-trending inliers separated by the Anti-Atlas Major Fault (AAMF) (Figure 1b), defining two structural domains [29]. The southwestern domain is dominated by Paleoproterozoic basement rocks [30], whereas the northeastern domain belongs to the Pan-African belt and exposes Neoproterozoic successions. Both domains are unconformably overlain by upper Ediacaran to Paleozoic sedimentary cover.

The Anti-Atlas basement consists of Paleoproterozoic crust (≈2.20–2.07 Ga) exposed mainly in the western and central sectors (Figure 1b), comprising metasedimentary rocks, paragneisses, migmatites, and granitoids [21,31–33]. The Taghdout Group (quartzites–carbonates–basalts), previously considered Neoproterozoic, is now partly reassigned to the late Paleoproterozoic based on intrusion by 1710 Ma and 1639 Ma doleritic dykes and sill complexes [31,34,35]. Mesoproterozoic activity is restricted to intraplate mafic magmatism documented by U–Pb dating of baddeleyite-bearing dykes [22,32,36].

Neoproterozoic rocks record the Pan-African cycle and are subdivided into four units [22,32]: (i) the Tachdamat–Bleïda Group (883 ± 2.3 Ma), a rift-related passive-margin sequence [35,37,38]; (ii) Bou Azzer–Siroua ophiolitic and arc assemblages [28,31,39–41]; (iii) lower Ediacaran siliciclastic basins of Saghro, Bou Salda, Anezi, and Tiddiline [25,42]; and (iv) the upper Ediacaran Ouarzazate Group, dominated by volcanic and plutonic rocks [21,43–46].

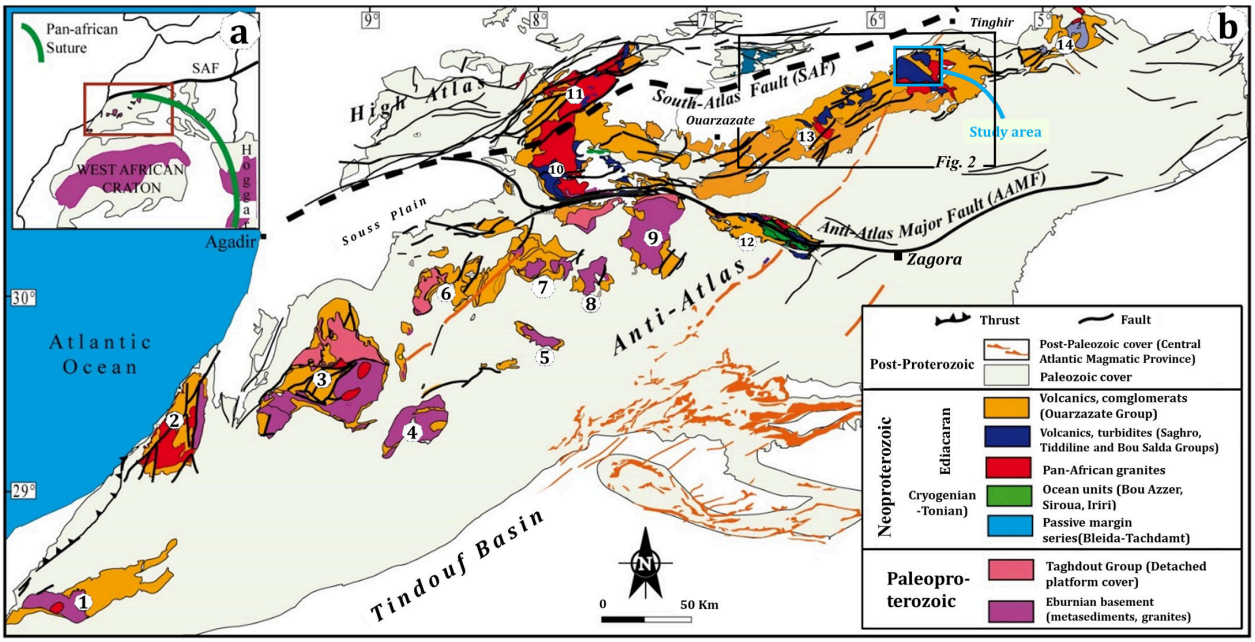


Figure 1. ((**a**), inset) Location of the Anti-Atlas at the northern margin of the West African Craton (WAC). (**b**) Geological map showing the distribution of the different Precambrian inliers in the Anti-Atlas belt including the Saghro massif. After [32], modified by [47]. The numbered Precambrian inliers shown on the map are: (1) Bas Drâa, (2) Ifni, (3) Kerdous, (4) Tagrara d'Akka, (5) Tagrara de Tata, (6) Ighrem, (7) Agadir Melloul, (8) Iguerda, (9) Zenaga, (10) Sirwa, (11) Ouzellagh, (12) Bou Azzer, (13) Saghro, and (14) Ougnat.

2.2. The Saghro Massif and the Imiter Sub-Inlier

The Saghro massif (Eastern Anti-Atlas; Figure 2) consists of a deformed lower Ediacaran siliciclastic basement (Saghro Group) affected by late Pan-African deformation [27,48], overlain unconformably by upper Ediacaran volcanic–plutonic rocks of the Ouarzazate Group [42,44–46,49]. These are locally overlain by Cambrian sedimentary sequences of the Taroudant–Tata Groups, with variable conformable to angular relationships [50,51].

The Saghro Group consists of up to 8000 m of low-grade metamorphosed siliciclastic and volcaniclastic sequences deposited in a marine basin [27]. Coeval arc magmatism is represented by the Bouskour andesites in the western Saghro domain [27]. Detrital zircon U–Pb data from Saghro Group rocks constrain the maximum depositional ages at 610 Ma and 604 ± 5 Ma, indicating a middle Ediacaran age [23,25,32]. However, the Igoudrane pluton, which intrudes the shale-dominated Tachkakkacht Formation of the Saghro Group, yields zircon crystallization ages of 677 ± 19 Ma [52] and 575 ± 10 to 538 ± 6 Ma [49]. These data imply that the deposition of the Saghro Group predates 677 Ma, prior to the emplacement of the pluton. Nevertheless, additional geochronological constraints are required to confirm the significance and reliability of the 677 Ma age.

The overlying Ouarzazate Group (580–550 Ma) forms a thick volcano–sedimentary and plutonic province emplaced during late Pan-African extension and magmatism [25,27,34,49,53] and is temporally associated with hydrothermal systems responsible for Ag mineralization in the Imiter district [54].

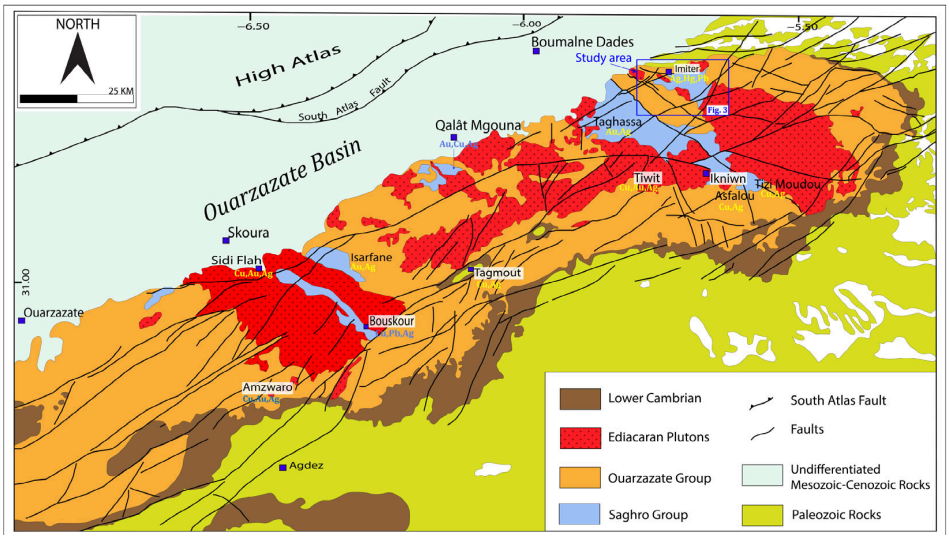


Figure 2. Simplified geological map of the Saghro Inlier. After [55], modified by [56]. Abbreviations: Ag, silver; Cu, copper; Au, gold; Hg, mercury; Pb, lead.

The Imiter Sub-inlier (NE Saghro; Figures 2 and 3) comprises deformed siliciclastic rocks of the Saghro Group hosting Hg–Ag mineralization [27,57,58] that are unconformably overlain by the Ouarzazate volcanic rocks while being intruded by late Ediacaran subvolcanic and plutonic bodies [25,27,45,48,59]. At Imiter, the Saghro Group comprises four stratigraphic formations, from base to top: (i) the Bou Teglimt Formation, dominated by sandstone; (ii) the Izemgane Formation, characterized by sandstones and shales; (iii) the Tachkakkacht Formation, consisting mainly of shales; and (iv) the Imiter Formation (the main focus of this study), which is predominantly composed of shales.

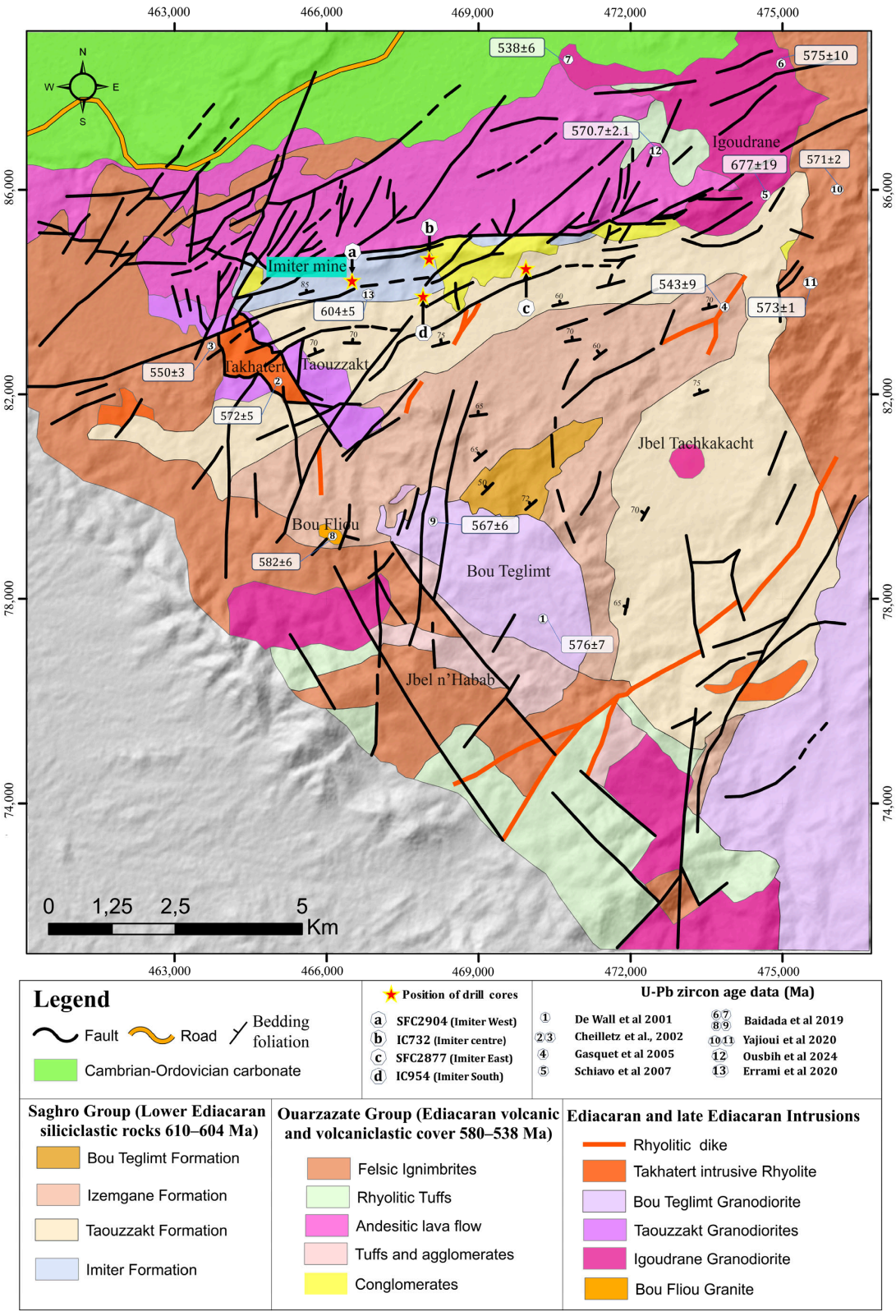


Figure 3. Geological map of the Imiter Sub-inlier after [26] and modified by [59,60], showing the location of the studied drill cores (a–d). The references listed in the legend (1–13) correspond to U–Pb zircon ages of igneous rocks from the Imiter Sub-inlier: (1) [61]; (2 and 3) [54]; (4) [62]; (5) [52]; (6, 7, 8 and 9) [60]; (10 and 11) [63]; (12) [64]; (13) [25].

3. Materials and Methods

3.1. Sampling

A total of 264 samples were obtained from drill cores obtained from four boreholes: SFC2904 (Imiter West; 63 samples), IC732 (Imiter Center; 47 samples), SFC2877 (Imiter East; 139 samples), and IC954 (Imiter South; 14 samples). The samples comprise shales and sandstones from the Imiter Formation of the Saghro Group. The locations of the four boreholes are shown in Figure 3, while the corresponding sampling depths are listed in Tables S1 and S2 of the Supplementary Materials. Detailed sampling intervals for each borehole are presented in Figure S1a–d of the Supplementary Materials. In addition, 20 surface samples reported by [27] were incorporated into the dataset for comparison.

3.2. Whole-Rock Geochemistry

Samples (1–2 kg each) were systematically collected along the four drill cores. Well-preserved, unaltered intervals with minimal evidence of fluid circulation were targeted to ensure representativeness of the primary sedimentary signatures. To minimize contamination, all samples were crushed and pulverized using agate mills.

Whole-rock geochemical analyses were performed on samples from three drill cores SFC2904 (Imiter West), IC732 (Imiter Center), and SFC2877 (Imiter East) at the Research, Mining and Exploration Centre (REMINEX) of Managem Group, Morocco. Samples from the IC954 drill core (Imiter South) were analyzed at Analytical Laboratory Services (ALS) Global Laboratories (North Vancouver, Canada), in collaboration with Carleton University, for major and trace elements, as well as rare earth elements (REEs).

At the Research, Mining and Exploration Centre (REMINEX), Managem Group (Morocco), powdered rock samples (~1000 mg) from the three drill cores (SFC2904, IC732, and SFC2877) were analyzed for major elements by X-ray fluorescence (XRF) using a MagiX XRF spectrophotometer was manufactured by PANalytical (B.V., Almelo, The Netherlands) equipped with a rhodium (Rh) target X-ray tube operated at 2.4 kW. Data acquisition and instrument control were performed using SuperQ: XRF Analysis Software (Version 3). Major element concentrations were determined on fused glass beads prepared by mixing the powdered samples with lithium tetraborate ($Li_2B_4O_7$) and lithium metaborate ($LiBO_2$), with lithium bromide (LiBr) added as a releasing agent. Fusion was carried out in platinum crucibles at 1200 °C, followed by cooling and casting into glass beads using platinum molds. Loss on ignition (LOI) was measured at 1000 °C prior to fusion.

Trace element concentrations were measured using inductively coupled plasma–atomic emission spectrometry (ICP–AES) with an Ultima 2C instrument (HORIBA Jobin Yvon, Longjumeau, France). Before analysis, 5 g of powdered sample was dried at 180 °C for 2 h. A representative aliquot (0.5 g) was then mixed with 2.5 g of sodium peroxide (Na_2O_2) in zirconium crucibles and fused at 450 °C for 45 min. The resulting melt was dissolved in a solution of 50 mL deionized water and nitric acid (HNO_3, 28–34%) prior to instrumental analysis. Full precision data are provided in Table S1 of the Supplementary Materials.

Additional geochemical analyses of drill core IC954 were conducted at ALS Global Laboratories (North Vancouver, Canada). Samples were fused and then dissolved in nitric acid. Major elements were determined by ICP–AES, while trace elements and rare earth elements (REEs) were determined using inductively coupled plasma–mass spectrometry (ICP–MS). Detailed analytical procedures, detection limits, and calibration protocols are available from ALS Global Laboratories (https://www.alsglobal.com) (accessed on 9 May 2026). Analytical quality control was maintained using internal and international reference materials, including a Carleton in-house basalt standard (10-LT-05) and the USGS reference material BHVO-2 [65,66]. Replicate analyses indicate analytical precision better than ±2%

for major elements and ±5% for trace and REEs. Full precision data are provided in Table S2 of the Supplementary Materials.

3.3. Sm Nd Isotopes

For Sm-Nd isotopic analysis, between 100 and 200 mg of sample powder (drill core IC954) is weighed into a screw-cap Teflon vial, to which a mixed ^{148}Nd–^{149}Sm spike is added. The powder–spike mix is dissolved in HNO_3-HF, then further attacked with HNO_3 and HCl until no residue is visible. The bulk REEs are separated by cation chromatography (Dowex 50-X8) using 2.5N HCl and 6N HCl. The REE-bearing residue is dissolved in 0.26N HCl and loaded into an Eichrom Ln-Spec chromatographic column containing Teflon powder coated with HDEHP [di(2-ethylhexyl) orthophosphoric acid; [67]]. Nd is eluted using 0.26N HCl followed by Sm in 0.5N HCl. All isotope ratios were determined on a Thermo-Finnigan NEPTUNE^{TM} MC-ICP-MS. Nd residue was dissolved in 2% HNO_3, and an aliquot was added to a 1.5 mL centrifuge tube containing 1 mL of 2% HNO_3 to yield a final concentration of 0.2 ppm. Isotope ratios are normalized to ^{146}Nd/^{144}Nd = 0.72190. Total procedural blanks for Nd are <100 picograms. The laboratory average ^{143}Nd/^{144}Nd for the JNdi-1 standard is 0.512085 +/− 0.000011 (n = 46, July 2019–August 2021), and all analyses have been normalized to the accepted value for the JNdi-1 standard of 0.512100 [68]. Analyses of the USGS standard BCR-2 yield Nd = 28.41 ppm, Sm = 6.53 ppm, and ^{143}Nd/^{144}Nd = 0.512626 + 0.000006 (n = 8). The BCR-2 sample analyzed in this study yielded ^{143}Nd/^{144}Nd = 0.512618 +/− 0.000007 and agrees well with accepted values [69]. All analytical uncertainties are 2-sigma standard deviations of the mean of ~90 scans. Sm residues were dissolved in 2% HNO_3, and an aliquot was added to a 1.5 mL centrifuge tube containing 1 mL of 2% HNO_3 to yield a final concentration of 0.2 ppm, followed by analysis with the MC-ICP-MS. Uncertainties in all Nd and Sm concentrations are +/− 1%, but uncertainties in the ^{147}Sm/^{144}Nd are <0.5% based on replicate runs (see Table S3 of the Supplementary Materials).

Epsilon values at time T are calculated using the following relation:

$$\varepsilon Nd(t) = [(^{143}Nd/^{144}Ndsample^{T}/^{143}Nd/^{144}NdCHUR^{T}) - 1] \times 10{,}000$$

where CHUR is the Chondrite Uniform Reservoir (0.512630) [70], the decay constant (λ) is 6.54×10^{-12} y^{-1}, and T is generally the time the rock was formed. Depleted mantle model ages (T_{DM}) are calculated assuming a modern upper mantle with ^{147}Sm/^{144}Nd = 0.214 and ^{143}Nd/^{144}Nd = 0.51315 [71]. The initial ^{143}Nd/^{144}Nd, εNd(t) values, and ages T_{DM} for the Imiter Formation were calculated using the depositional age of t = 604 Ma based on data from [23,25].

3.4. Total Organic Carbon (TOC) and Organic Carbon Isotope ($\delta^{13}C_{org}$) Measurements

To quantify organic carbon abundance and composition, total organic carbon (TOC) content and organic carbon isotopic compositions ($\delta^{13}C_{org}$) were measured on 14 shale and sandstone samples collected at different depths from drill core IC954 within the Imiter Formation of the Saghro Group, south of the Imiter silver mine (see Table S4 of the Supplementary Materials). This core was selected due to its relatively distal position from the mining area, which minimized potential overprinting by hydrothermal fluid circulation.

Total organic carbon (TOC) concentrations and carbon isotope ratios were measured at the Department of Earth and Planetary Sciences, University of California, Riverside (USA), using a Costech 4010 Elemental Analyzer (EA) coupled to a Thermo-Finnigan Delta V Advantage isotope-ratio mass spectrometer via an open-split interface (ConFlo IV, Thermo-Finnigan, Somerset, NJ, USA). C isotope ratios are reported in delta notation and per mil units relative to international standards on the Vienna Pee Dee Belemnite (V-PDB) scale.

Sample normalization was performed using the two-point calibration described in [72]. Two intralaboratory standards (acetylene and glycine) were analyzed before, between, and after unknowns in each run. A calibration line was calculated for each run by least-squares linear regression using the known and measured carbon isotope values of the calibration standards. To monitor the quality of sample preparation and analysis performance, the international standard USGS Devonian Shale SDO-1 ($\delta^{13}C_{org} = -30.0 \pm 0.1$‰ V-PDB) was treated and analyzed as an unknown. Replicate analyses of the SDO-1 standard yielded the $\delta^{13}C_{org}$ value of -30.0 ± 0.1‰ ($n = 24$). Samples were analyzed in triplicate, and average values are reported in Table S4 of the Supplementary Materials.

$$\delta^{13}C\ (‰) = [(({}^{13}C/{}^{12}C)_{Corganic}/({}^{13}C/{}^{12}C)_{VPDB}) - 1] \times 1000$$

3.5. Data Analysis and Geochemical Proxies

The geochemical data were processed using ioGAS^{TM} Geochemistry Software (Iogas 8.3.1) (https://www.imdex.com/software/iogas). One of the main objectives of the whole-rock geochemistry was to evaluate key geochemical proxies providing constraints on provenance and recycling, paleoclimate and paleoweathering, and redox conditions [73].

This study integrates multiple complementary geochemical proxies to assess rock composition and to reconstruct both depositional and post-depositional processes.

The Al_2O_3/TiO_2 ratio was employed to estimate the SiO_2 content of the source rocks using the equation of [74]: SiO_2 (wt.%) = 39.34 + 1.2578 (Al_2O_3/TiO_2) − 0.0109 (Al_2O_3/TiO_2)^2.

The Index of Compositional Variability (ICV) was calculated to quantify compositional heterogeneity among major oxides. The ICV was computed as:

ICV = (Fe_2O_3 + K_2O + Na_2O + CaO + MgO + MnO)/Al_2O_3 [75].

Chemical weathering intensity was evaluated using the Chemical Index of Alteration (CIA) [13]:

CIA = 100 × [Al_2O_3/(Al_2O_3 + CaO* + Na_2O + K_2O)].

where CaO* represents the silicate fraction of calcium, corrected as:

CaO* = min [CaO − (10/3)P_2O_5, Na_2O] [4,13].

Plagioclase Index of Alteration (PIA) is measured as:

PIA= [(Al_2O_3 − K_2O)/(Al_2O_3 + CaO* + Na_2O)] × 100 [76].

In addition, the Chemical Index of Weathering (CIW) [77] was used to further constrain weathering processes:

CIW = [Al_2O_3/(Al_2O_3 + CaO* + Na_2O)] × 100.

Whole-rock geochemistry provides widely used proxies for reconstructing redox conditions in sedimentary environments, based on the behavior of redox-sensitive elements and their enrichment relative to detrital background. Commonly used elemental ratios include V/Cr, V/(V + Ni), Ni/Co, and U/Th. High values of V/Cr, V/(V + Ni), and Ni/Co are generally associated with reducing-to-anoxic depositional conditions, whereas elevated U/Th ratios typically indicate authigenic uranium enrichment under low-oxygen environments [78–83].

Together, these approaches provide a robust framework for interpreting sediment provenance, the extent of sediment recycling, weathering intensity, and prevailing paleoclimatic conditions.

4. Results

4.1. Drill Core Logging and Stratigraphic Correlation

Near the Imiter silver mine, the Imiter Formation of the Saghro Group is dominated by siliciclastic deposits. These successions, although only mildly deformed, comprise approximately 2000 to 8000 m of flysch-like turbiditic sequences [26]. These successions are

characterized by a pervasive schistosity [48] and comprise two main facies associations: dominant shales and subordinate sandstones.

Figure 4a illustrates the typical surface expression of these rocks, whereas Figure 4b–d shows their subsurface appearance in drill cores (borehole IC954, Imiter South). Figure 5 presents the stratigraphic columns logged from the drill cores through the Imiter Formation, from west to east: borehole SFC2904 (Imiter West), borehole IC732 (Imiter Center), borehole SFC2877 (Imiter East), and borehole IC954 (Imiter South). These logs reveal a regionally developed unconformity separating the conglomerates of the overlying 580–538 Ma Ouarzazate Group from the underlying shales and sandstones of the 610–604 Ma Imiter Formation. The Imiter Formation is locally intruded by mafic-to-andesitic dykes and granitoid bodies.

The drill core from borehole SFC2904 (Imiter West), with a thickness of 62.5 m, is dominated by shales and fine-grained sandstones, particularly toward the upper part of the succession. It is notably enriched in argentiferous mineralization. Borehole IC732 (Imiter Center), with a thickness of 124 m, is also predominantly composed of shales and locally cuts mafic and andesitic dykes ranging in thickness from approximately 3 m to 15 m. It is also notably enriched in argentiferous mineralization. Borehole SFC2877 (Imiter East), with a total thickness of 326.5 m, is characterized by coarse-grained sandstones at its base. This succession also includes mafic dykes as well as a meter-scale granitoid intrusion. Borehole IC954 (Imiter South), with a thickness of 151 m, is dominated by shales at its base and by sandstones toward the top, and it also contains a few mafic dykes.

Stratigraphic correlations are primarily established between the three northern and central boreholes (SFC2904, IC732, and SFC2877), which display broadly comparable lithostratigraphic architectures. By contrast, borehole IC954 (Imiter South) is more difficult to correlate with the others due to its more distal southern position and its distinct lithological succession.

4.2. Petrography and Mineralogy of Imiter Shales and Sandstones

Shale samples are predominantly composed of quartz, feldspar, and biotite, with minor amounts of pyrite locally observed. Quartz occurs in both monocrystalline and polycrystalline forms and is the most abundant mineral phase. Potassium feldspars (orthoclase, microcline, and perthite) are less common than plagioclase. Lithic fragments derived from plutonic, sedimentary, and metamorphic sources are also present. Muscovite is a common accessory mineral, accompanied by subordinate phases such as apatite, zircon, tourmaline, and titanium oxides (see Figure 6).

The sandstone samples are dominated by fine-grained (60–65%), typically sub-angular quartz grains exhibiting straight to undulatory extinction. Feldspars (orthoclase and plagioclase) are present but commonly exhibit signs of alteration. Lithic fragments make up approximately 10–15% of the framework. A fine-grained matrix envelops the detrital grains and occupies the spaces between them, which points to strong mechanical compaction.

Petrographic observations also reveal a well-developed slaty cleavage (S_1), oriented parallel or slightly oblique to the primary sedimentary bedding (S_0). This cleavage develops within a fine-grained matrix that shows textural heterogeneity across different microstructural domains.

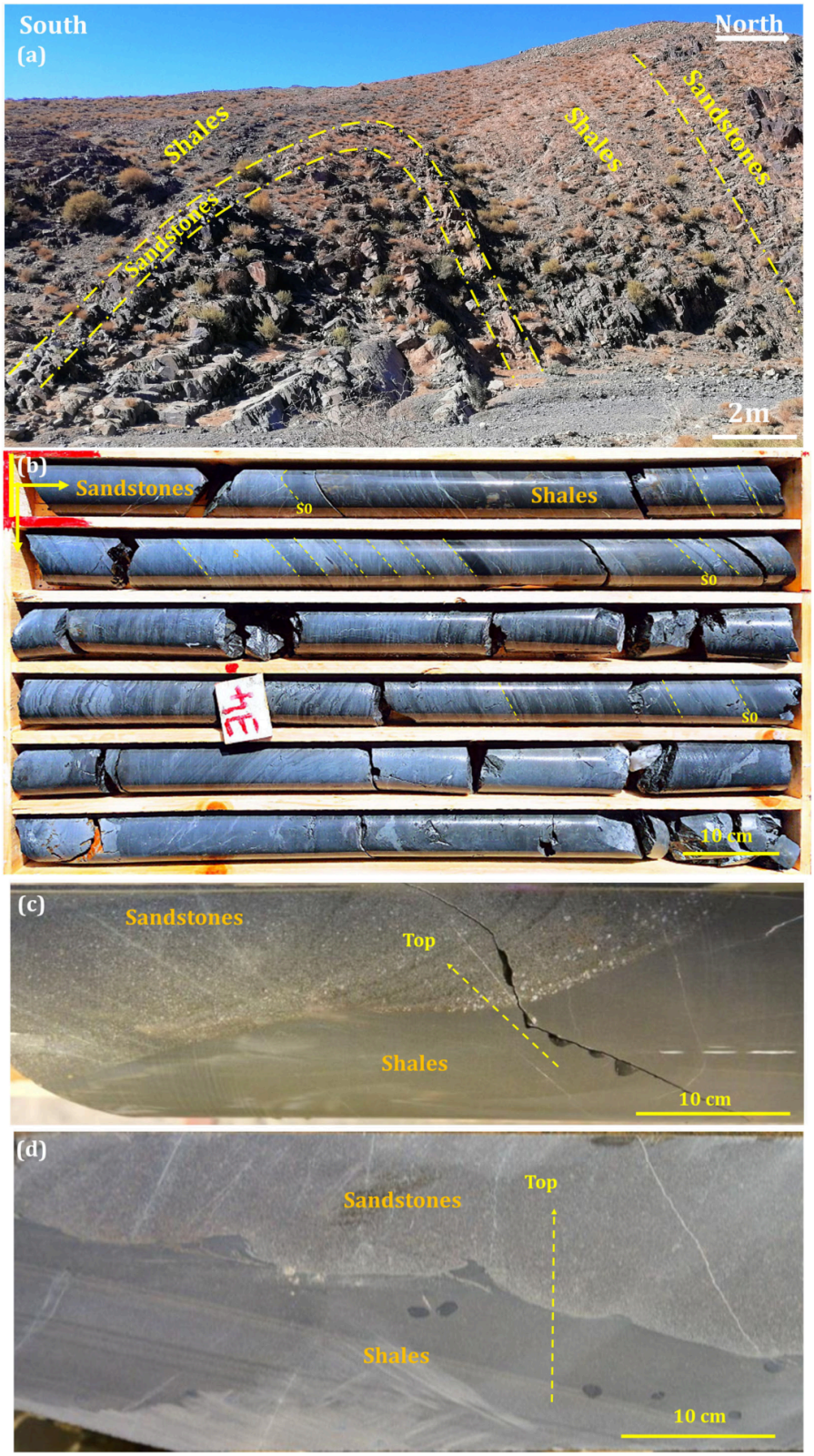


Figure 4. (**a**) Typical outcrop appearance of the Imiter Formation of the Saghro Group near the Imiter silver mine. (**b**) Representative drill core from the Imiter Formation (borehole IC954, Imiter South). The yellow arrow points to the top of the drill core. (**c**) Erosive surface and crossbedding between shale and sandstone. (**d**) Erosive surface between shale and sandstone. The dashed arrow indicates the top of the sequence. Abbreviations: S0, bedding. The number 34 in red indicates the borehole depth (34 m).

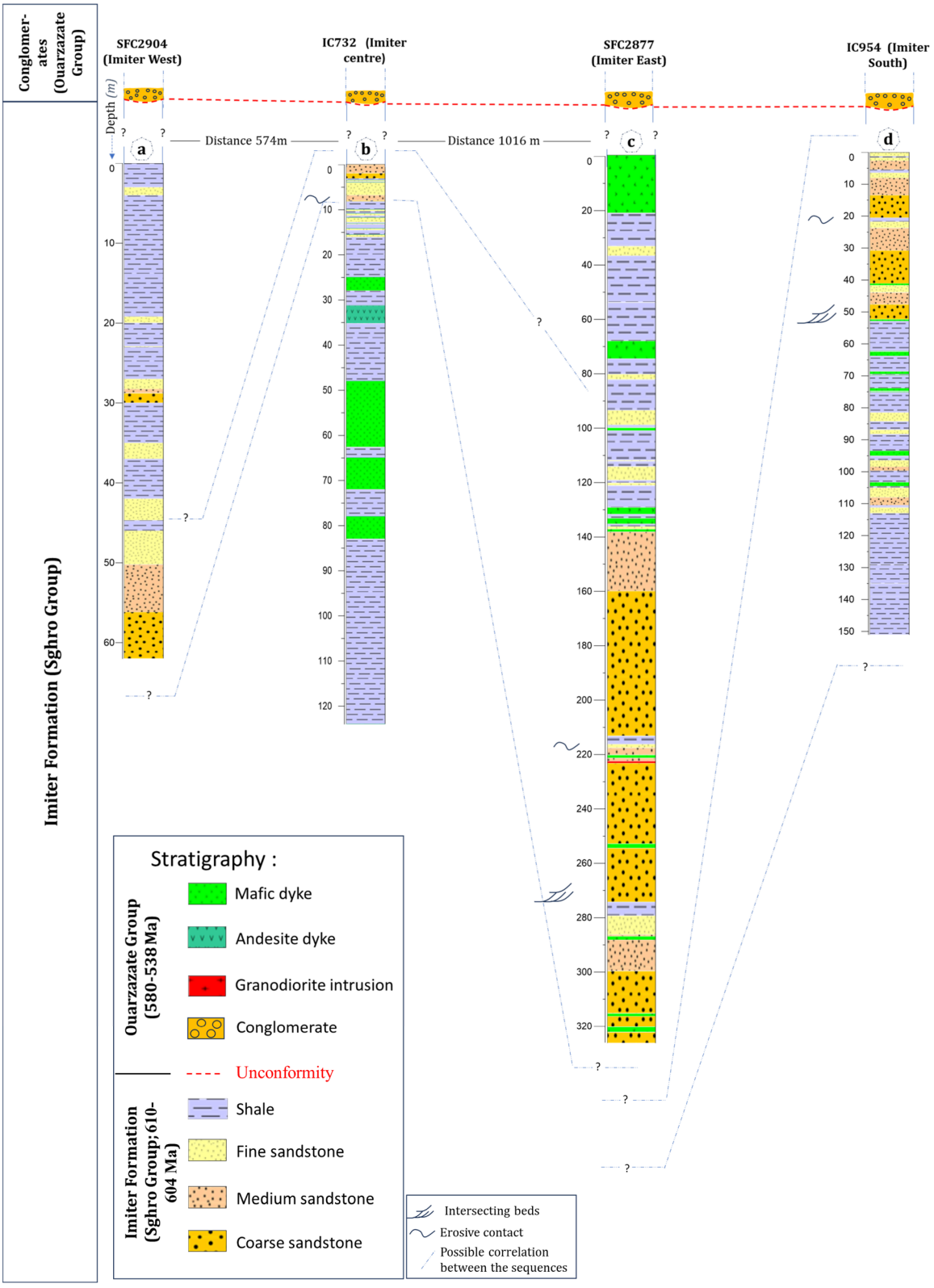


Figure 5. Stratigraphic columns logged from drill cores through the Imiter Formation of the Saghro Group in the Imiter Sub-inlier, from west to east: borehole SFC2904 (Imiter West), borehole IC732 (Imiter Center), borehole SFC2877 (Imiter East), and borehole IC954 (Imiter South). The locations of the boreholes are provided in Figure 3 and Tables S1 and S2 of the Supplementary Materials. The stratigraphic positions of all analyzed samples are displayed on the borehole logs in Supplementary Figure S1a–d.

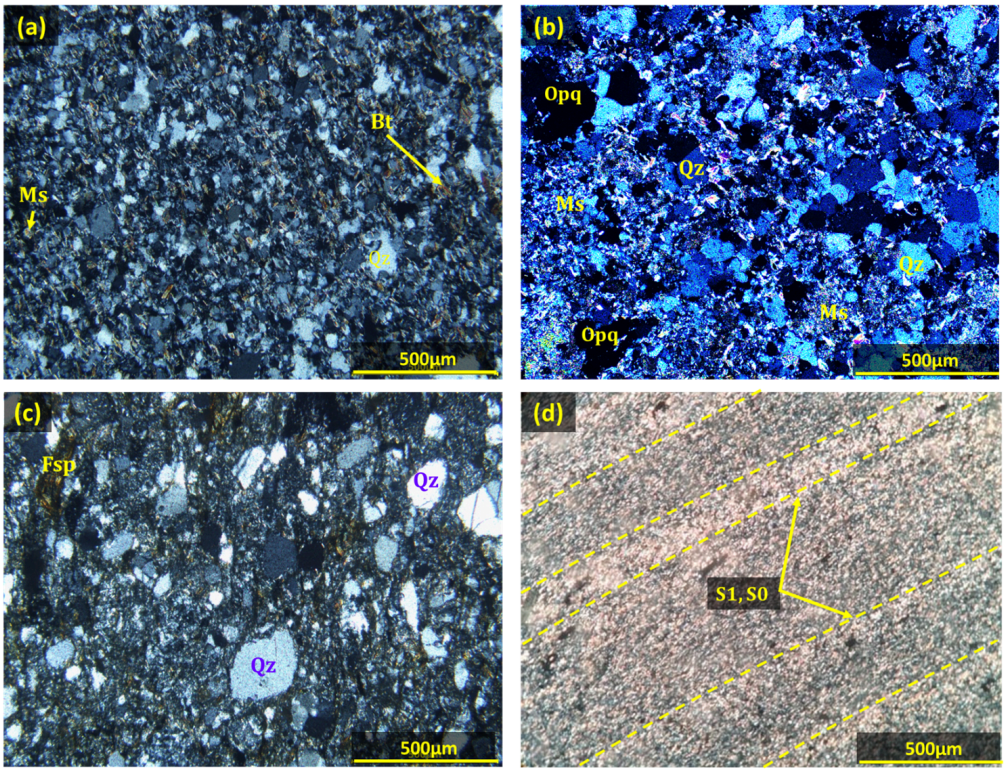


Figure 6. Thin section under optical microscope illustrating the textures of shales and sandstones from the Imiter Formation of the Saghro Group in the Imiter Sub-inlier. (**a**) Fine-grained sandstone; (**b**) medium-grained sandstone; (**c**) coarse-grained sandstone; (**d**) shale. (**a**–**c**): Cross-polarized light images; (**d**): plane-polarized light images. Abbreviations: S1, schistosity; S0, bedding; Qz, quartz; Bt, biotite; Ms; muscovite; Opq, opaque mineral; Fsp, feldspar according to [84].

4.3. Elemental Geochemistry and Sm-Nd Isotopes of Imiter Shales and Sandstones

4.3.1. Major Elements

The distribution of the Imiter Formation samples on the Herron diagram [77] is shown in Figure 7. Most samples are classified as shales and wackes, with a limited number plotting in the Fe-shale, litharenite, and sublitharenite fields. Surface samples reported by [27] are mainly distributed within the arkose field.

The major element compositions of shales and sandstones from the Imiter Formation (Saghro Group, Eastern Anti-Atlas) are provided in Tables S1 and S2 of the Supplementary Materials. SiO_2 (~39.9–75.1 wt.%) shows a wide range, with a higher content in sandstones (>60%) and lower, more variable values in shales, whereas Al_2O_3 (~4.1–21.5 wt.%) is relatively enriched in shales. Fe_2O_3 (~0.2–11.6 wt.%) and MgO (~0.6–11.4 wt.%) display broad variability without clear lithological control. CaO (~0.3–19.3 wt.%) is generally low but locally elevated, while alkali oxides are variable, with K_2O (~0.01–6.1 wt.%) slightly higher in shales and Na_2O (~0.01–5.8 wt.%) showing no systematic trend. TiO_2 (~0.15–1.03 wt.%) and P_2O_5 (~0.07–2.77 wt.%) remain low, and MnO (~0.02–0.71 wt.%) is minor. The major element composition is dominated by SiO_2 and Al_2O_3, whereas Fe_2O_3, MgO, and alkali oxides occur in lower proportions. Variations in oxide abundances are observed between the shale and sandstone samples.

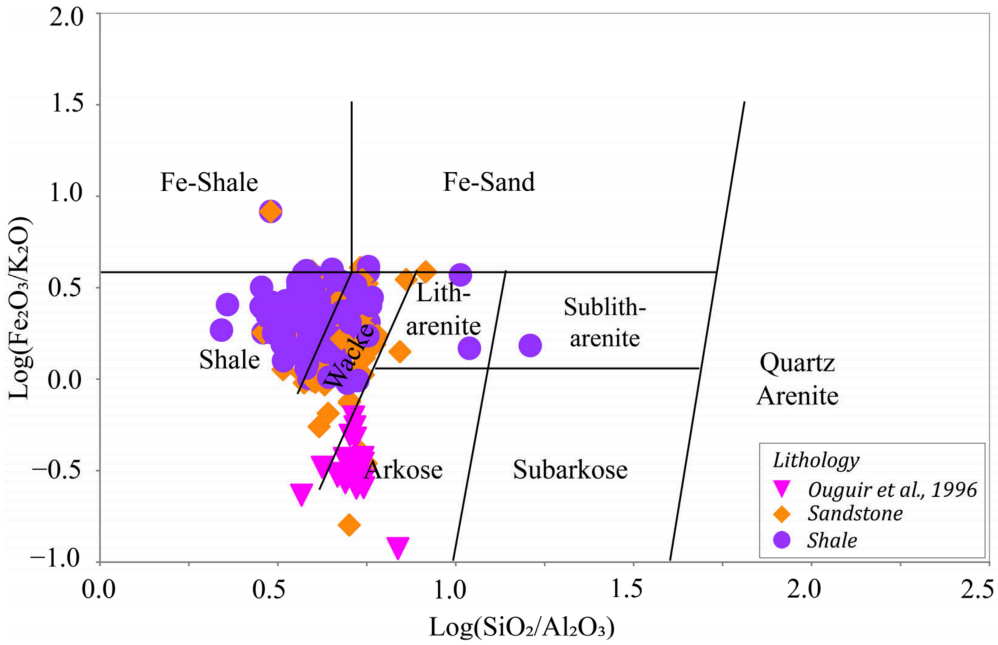


Figure 7. Geochemical classification diagram of siliciclastic rocks from the Imiter Formation (after [77]). Literature data were taken from Ouguir et al. (1996) [27].

4.3.2. Trace Elements

To assess variations in trace element concentrations in shales and sandstones of the Imiter Formation, values of the upper continental crust (UCC) [20] were used as a reference. The data in Tables S1 and S2 of the Supplementary Materials show significant variability relative to UCC.

Lithophile large-ion elements (LILEs), including Rb, Ba, and Sr, exhibit contrasting distributions. Rubidium (~34–108 ppm) and barium (~4.1–1958 ppm) are generally enriched in shales relative to the upper continental crust (UCC), whereas strontium (~0.6–509 ppm) shows no systematic enrichment or depletion. High-field-strength elements (HFSEs), including Zr (~0.3–478 ppm), Hf (~4.45–5.45 ppm), Nb (~4–55 ppm), and Th (~6–155 ppm), display a wide concentration range. Sandstone samples show higher Zr and Hf concentrations than UCC values, whereas shale samples display lower enrichments. Transition elements, such as Cr (~0.5–285 ppm), Ni (~0.2–951 ppm), and V (~0.5–213 ppm), show variable abundances, locally exceeding crustal averages.

Taken together, the trace element systematics reveal a non-uniform pattern of enrichment and depletion relative to UCC standards. Shale and sandstone samples display distinct trace element distributions, with systematic differences in the abundance of several immobile trace elements.

4.3.3. Rare Earth Elements (REEs)

The data on rare earth elements (REEs) presented here are derived exclusively from samples taken from drill core IC954, located in the southern part of the Imiter silver mine.

The samples show relatively high total rare earth element (ΣREE) concentrations, ranging from 114.33 to 216.22 ppm, with an average of 170.92 ppm. Heavy rare earth elements (ΣHREEs) range from 28.28 to 55.18 ppm, with an average of 39.3 ppm, while light rare earth elements (ΣLREEs) exhibit a wider range, from 86.05 to 176.68 ppm, with an average value of 131.6 ppm.

When normalized to the Post-Archean Australian Shale (PAAS) [3], the REE patterns (Figure 8a) display relatively uniform distributions with moderate fractionation. By con-

trast, normalization to the upper continental crust (UCC) [20] (Figure 8b) reveals greater variability among the samples.

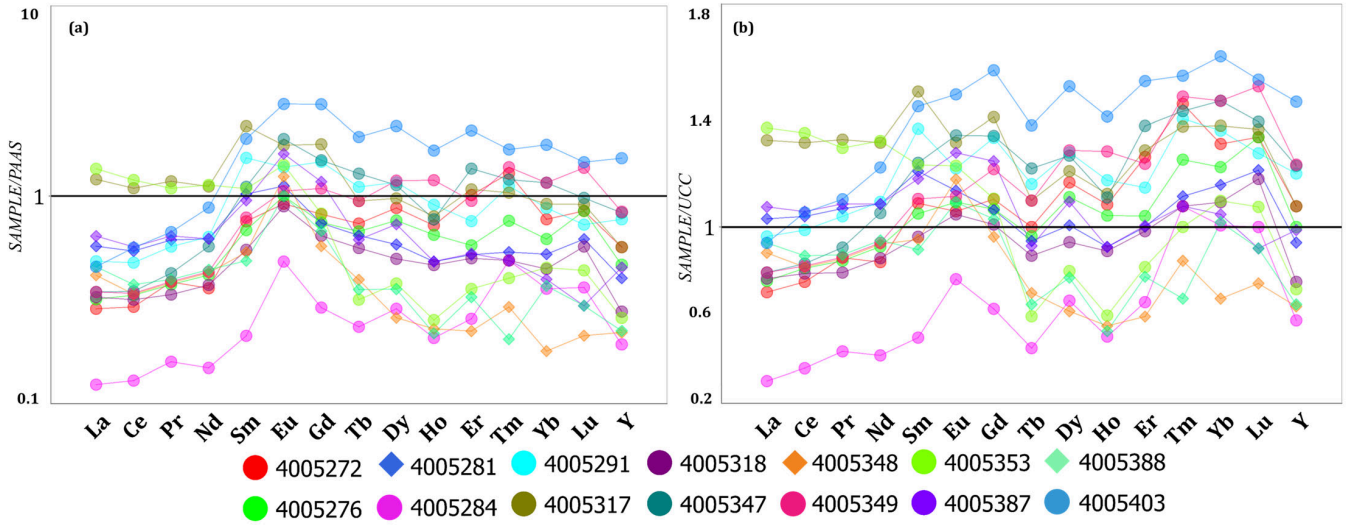


Figure 8. Rare earth element distributions of Imiter sandstones and shales from drill core IC954 (Imiter South), normalized to (**a**) Post-Archean Australian Shale Composite (PAAS) [3] and (**b**) upper continental crust (UCC) [20]. All samples are shales, except for samples 4005281, 4005348, 4005387, and 4005388, which are sandstones.

Overall, the REE patterns are characterized by coherent trends with limited dispersion. Most samples plotted are shale lithologies, except for samples 4005281, 4005348, 4005387, and 4005388, which are identified as sandstones. The PAAS-normalized REE patterns are characterized by low La/Sm ratios and a gradual decrease from light rare earth elements (LREEs) to heavy rare earth elements (HREEs). Most samples show weak-to-absent Eu anomalies, whereas a few samples display positive Eu anomalies. Furthermore, HREE concentrations appear to be relatively more enriched in the UCC than in the PAAS. REE patterns normalized to PAAS and UCC display different amplitudes of variation among the samples.

4.3.4. Sm-Nd Isotopes

The Sm–Nd isotopic compositions of samples from borehole IC954 are reported in Table S3 of the Supplementary Materials. The isotopic data show limited variability and no systematic distinction between sandstone and shale lithologies. Initial $^{143}Nd/^{144}Nd$ ratios range from 0.511424 to 0.511542 (mean = 0.511491), while $^{147}Sm/^{144}Nd$ ratios vary from 0.095041 to 0.131198 (mean = 0.116729).

All samples display negative εNd(t) values ranging from −6.21 to −8.50, with corresponding T_{DM} model ages between 1.58 and 2.09 Ga and $f^{Sm/Nd}$ values from −0.5168 to −0.3330 (Table S3 of the Supplementary Materials).

Despite the overall isotopic homogeneity, subtle geochemical differences are observed between lithologies. Sandstones are characterized by a higher SiO_2 content, stronger enrichment in light rare earth elements (LREEs; reflected by higher La/Yb and ΣLREE/ΣHREE ratios), and slightly more negative εNd(604 Ma) values compared to shales (Figure 9a,b). The T_{DM} model ages are broadly similar for both the shale and sandstone samples, ranging from approximately 1.6 to 2.0 Ga.

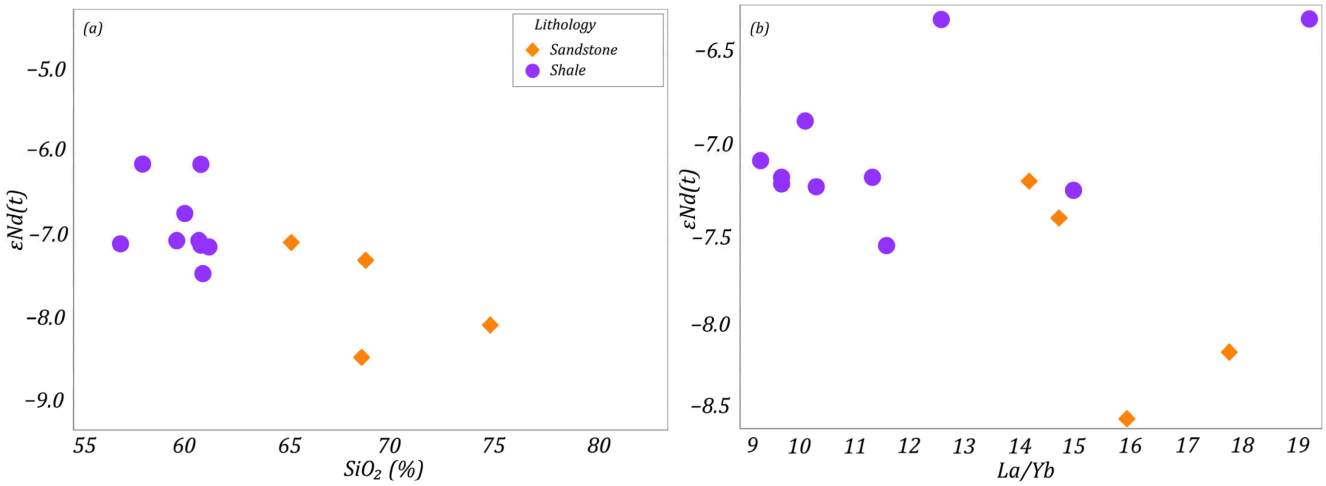


Figure 9. (**a**) εNd(t) versus SiO_2 and (**b**) εNd(t) versus La/Yb for shale and sandstone samples from borehole IC954 (Imiter South). Uncertainty in εNd(t) is ~=/− 0.3 epsilon units.

No systematic relationship is observed between εNd(t) values and either La/Yb or ΣLREE/ΣHREE ratios.

4.3.5. Total Organic Carbon (TOC) and Organic Carbon Isotope ($\delta^{13}C_{org}$)

Total organic carbon (TOC) content and organic carbon isotopic compositions ($\delta^{13}C_{org}$) were determined for 14 samples collected at different depths from drill core IC954 within the Imiter Formation (Saghro Group), located south of the Imiter silver mine (see Table S4 in the Supplementary Materials).

Total organic carbon (TOC) content is uniformly low, ranging from 0.1 to 0.3 wt.% in all analyzed samples. The $\delta^{13}C_{org}$ values range from −27.7 to −25.6‰ (VPDB).

5. Discussion

5.1. Sediment Provenance and Crustal Evolution

5.1.1. Geochemical Constraints on Provenance, Sedimentary Processes and Source Composition

The integrated whole-rock geochemical dataset, including major, trace, and rare earth elements, provides a robust framework for evaluating sediment provenance and depositional processes [85]. The distribution of the Imiter Formation samples on the Herron diagram is dominated by shale and wacke compositions, with only a few samples plotting within the Fe-shale, litharenite, and sublitharenite fields. By contrast, surface samples reported by [27] are predominantly classified as arkoses. This contrast suggests compositional differences between the drill-core and surface datasets. The shale- and wacke-dominated compositions of the drill core samples indicate a greater abundance of aluminosilicate-rich material, whereas the arkosic compositions observed in surface exposures imply a stronger contribution from feldspar-rich detritus. Such variations may reflect lithological heterogeneity within the basin, changes in sediment supply, or differences in the stratigraphic intervals and depositional environments represented by the sampled successions.

To further constrain source-rock composition, the Al_2O_3/TiO_2 ratio is commonly used as a provenance indicator because Al and Ti are relatively immobile during weathering, transport, and diagenesis [86]. In igneous rocks, Al is largely associated with feldspars, whereas Ti is mainly hosted in ferromagnesian minerals such as biotite, ilmenite, pyroxene, and amphibole. Consequently, Al_2O_3/TiO_2 ratios generally increase with increasing silica content and can be used to discriminate between felsic, intermediate, and mafic source

rocks [74,87]. Felsic rocks (66–76 wt.% SiO_2) typically exhibit Al_2O_3/TiO_2 ratios of 21–70, intermediate rocks (53–66 wt.% SiO_2) ratios of 8–21, and mafic rocks (<52 wt.% SiO_2) ratios of 3–9.

Figure 10 presents two complementary discrimination diagrams used to constrain the bulk composition and provenance of the Imiter siliciclastic rocks. In the SiO_2 versus Al_2O_3/TiO_2 diagram (Figure 10a), most shale samples form a coherent cluster within the intermediate compositional field ($SiO_2 \approx 52$–62 wt.%), with only limited variation in Al_2O_3/TiO_2 ratios. A few samples extend toward a lower SiO_2 content, approaching the mafic field. By contrast, the sandstone samples consistently display higher SiO_2 values (≈65–75 wt.%) and plot mainly within the felsic domain, although with slightly greater variability in Al_2O_3/TiO_2 ratios. The literature data from [27] closely match the new dataset, supporting the consistency of these compositional trends in the drill cores.

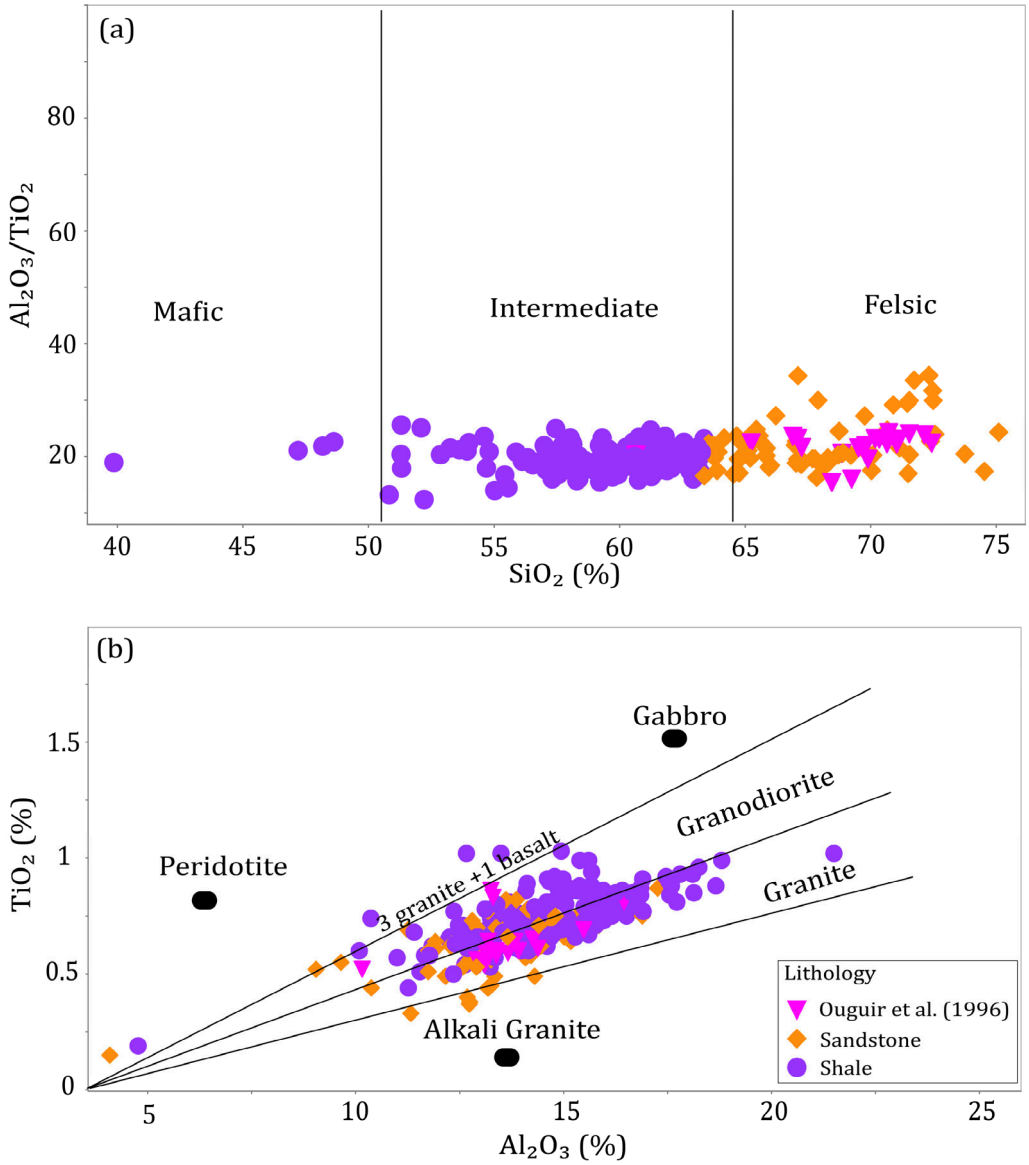


Figure 10. Provenance diagrams for the Imiter siliciclastic rocks. (**a**) The Al_2O_3/TiO_2 (wt %) versus SiO_2 (wt %) bivariate diagram of [88]. The mafic, intermediate and felsic fields based on SiO_2 are from [89]. (**b**) The TiO_2 (wt %) versus Al_2O_3 (wt %) diagram of [90]. The "granite line" and "3 granite + 1 basalt line" are after [91]. Literature data were taken from [27].

The Al_2O_3–TiO_2 diagram (Figure 10b) further refines these interpretations. Most shale and sandstone samples define a well-constrained linear trend between granodioritic and granitic compositions. Only a small number of samples show a slight shift toward the mafic to ultramafic fields, without reaching gabbroic or peridotitic end members. Overall, the absence of strong ultramafic or mafic signatures, together with the clustering of samples near the granodiorite–granite trends, points to a predominantly felsic source for the Imiter sediments.

Taken together, these geochemical discrimination diagrams indicate that the sediments of the Imiter Formation were predominantly derived from intermediate-to-felsic upper continental crustal sources, with a substantial contribution from granitoid rocks. The shale samples exhibit a more homogeneous geochemical composition, reflecting a well-mixed and compositionally averaged source dominated by upper crustal inputs, with only a minor influence of sediment recycling and reworking. By contrast, the sandstones preserve a stronger felsic signature, which suggests a greater contribution from proximal felsic source rocks and less compositional homogenization during transport and deposition.

The lack of significant overlap with mafic or ultramafic fields indicates that juvenile, mantle-derived sources played only a minor role in sediment supply. Instead, the geochemical trends point to erosion of the evolved continental crust, including granodioritic to granitic terranes. The slight shift in some samples toward mafic and ultramafic fields may reflect minor inputs from intermediate igneous rocks or variations in heavy mineral concentration during transport and sediment sorting.

Overall, Figure 10 supports a model in which the Imiter basin was primarily fed by detritus derived from evolved continental crust, consistent with an upper crustal provenance and very limited contribution from primitive or oceanic sources.

Immobile trace elements such as Th, Sc, Zr, and Hf are widely used in provenance studies because they are relatively resistant to chemical weathering, diagenesis, and low-grade metamorphism [92]. Enrichment in Zr and Hf is commonly associated with zircon concentration during sediment recycling, whereas sedimentary reworking is reflected by the increased compositional and textural maturity of the siliciclastic sediments.

Figure 11 presents three complementary trace element discrimination diagrams that provide insights into source-rock composition, provenance variability, and sediment recycling within the Imiter Formation.

In the Th/Sc versus Zr/Sc diagram (Figure 11a), the samples define a coherent trend characterized by low-to-moderate Zr/Sc ratios and progressively increasing Th/Sc values. Most shale and sandstone samples plot between mafic and felsic end members, whereas the literature data from [27] are displaced toward the felsic domain, indicating a stronger upper continental crust signature. The limited spread along the Zr/Sc axis suggests only minor zircon enrichment and, consequently, a low degree of sediment recycling. The overall trend is primarily controlled by source-rock composition rather than by zircon accumulation during repeated recycling. Samples from borehole IC954 cluster near the felsic end member and show no clear evidence of recycling, while several samples from [27] exhibit higher Zr/Sc ratios, reflecting a greater influence of zircon-rich recycled material.

The Co/Th versus La/Sc diagram (Figure 11b) further constrains source-rock composition. Most Imiter samples fall within the felsic field and are clearly separated from basaltic and andesitic compositions, indicating a dominant felsic contribution with only limited input from intermediate-to-mafic sources. The relatively tight clustering of shale samples suggests a more homogeneous provenance than the slightly more dispersed sandstone population, which may reflect minor source mixing or grain-size-dependent sorting effects.

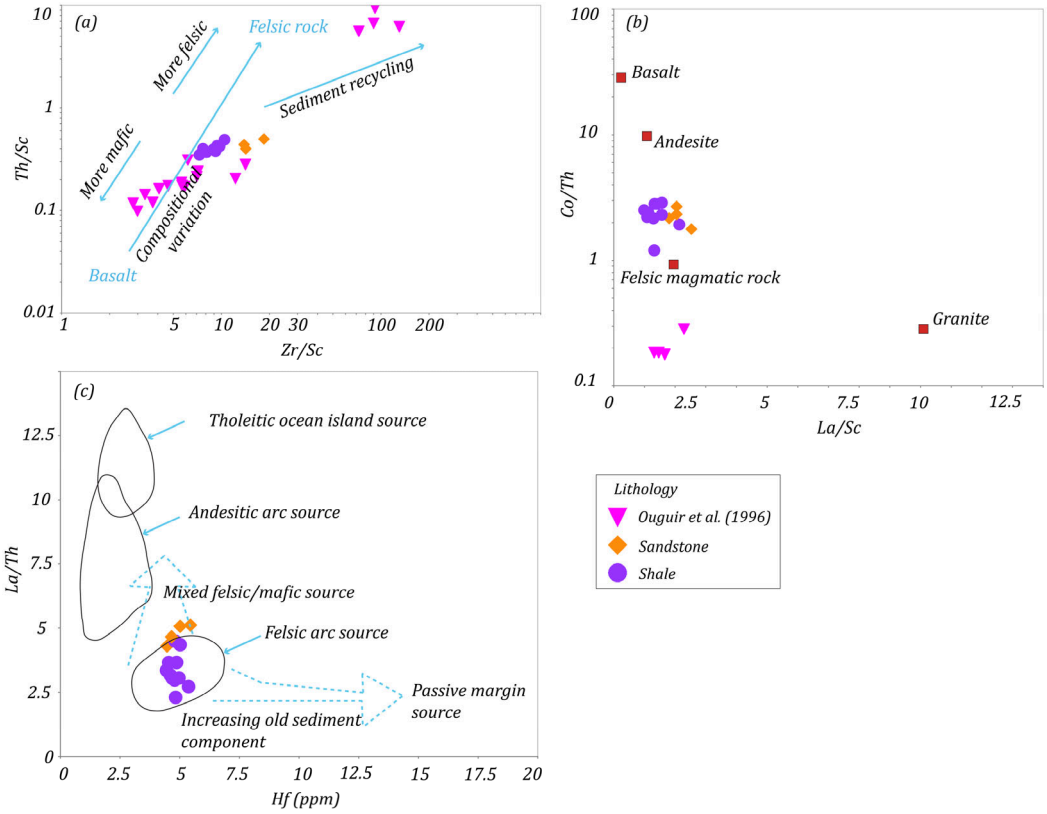


Figure 11. Trace element compositional attributes of siliciclastic rocks of Imiter Formation from drill core IC954 (Imiter South), compared with literature data from [27]. (**a**) Th/Sc-Zr/Sc (ppm) discrimination diagram [93]. (**b**) Co/Th-La/Sc (ppm) discrimination diagram (modified after [94]). (**c**) La/Th-Hf (ppm) discrimination diagram [95].

The La/Th versus Hf diagram (Figure 11c) provides additional constraints on both provenance and recycling. Most samples plot within or close to the felsic arc field, although a few extend toward the mixed felsic–mafic domain. Their generally low Hf content and moderate La/Th ratios are consistent with derivation from felsic igneous sources and limited heavy mineral enrichment.

The absence of a clear shift toward the passive-margin field suggests that extensive sediment recycling and derivation from mature cratonic sources were not dominant. Instead, the data point to relatively proximal source areas, likely associated with an active continental margin or arc-related setting.

Overall, the geochemical discrimination diagrams indicate that the siliciclastic rocks of the Imiter Formation were derived predominantly from felsic upper continental crustal sources, with minor contributions from intermediate arc-related lithologies and subordinate mafic inputs. The limited zircon enrichment observed in some samples suggests only minor sediment recycling and reworking. These characteristics are consistent with the erosion of felsic arc-related crust within an active-margin setting.

The PAAS-normalized REE patterns are consistent with a predominantly felsic crustal source. Although a few samples display positive Eu anomalies, likely reflecting minor contributions from feldspar-rich detritus or Ediacaran volcanic material, their limited occurrence suggests only a negligible influence on the overall provenance signature. The greater variability of the UCC-normalized patterns indicates subtle differences in source composition and sedimentary evolution. Part of this contrast may result from differences in zircon abundance between the PAAS and UCC reference compositions, particularly affecting the distribution of heavy rare earth elements.

5.1.2. Sm–Nd Isotopic Constraints on Sediment Provenance and Crustal Evolution

The Sm–Nd isotopic data provide important constraints on the sediment provenance and crustal evolution of the Imiter Basin [4,96,97]. Figure 12a shows the relationship between the εNd(t) values and Nd model ages (T_{DM}) for the Imiter samples analyzed in this study, together with representative igneous and metasedimentary rocks from the Anti-Atlas inliers. The comparable T_{DM} model ages obtained for both the shale and sandstone samples suggest derivation from crustal sources sharing a similar long-term evolutionary history. Moreover, the lack of correlation between εNd(t) and REE fractionation indices (La/Yb and ΣLREE/ΣHREE) indicates that the Nd isotopic compositions primarily reflect source characteristics rather than fractionation processes.

The Imiter samples are characterized by consistently negative εNd(t) values (−8.5 to −6.2) and Paleoproterozoic T_{DM} model ages (~1.7–2.1 Ga). Together, these isotopic features indicate a dominant contribution from ancient continental crust, consistent with derivation from the West African Craton and its recycled crustal derivatives, with little evidence for significant juvenile mantle input.

The clustering of the Imiter Formation data within the Paleoproterozoic field, close to the compositions of Kerdous granitoids and metapelites, suggests that these lithologies were the primary sediment sources. By contrast, more radiogenic εNd(t) values (≥0) observed in some Zenaga and Bas Drâa granitoids reflect more juvenile crustal inputs, which are only weakly represented in the Imiter sediments. The lack of strongly positive εNd(t) values further indicates that direct contributions from depleted mantle-derived material during sedimentation were minimal.

Figure 12b further refines this interpretation using the $f^{Sm/Nd}$ versus εNd(t) diagram [98]. The Imiter samples show negative $f^{Sm/Nd}$ values (−0.5 to −0.3), together with negative εNd(t), and plot mainly within or close to the field of LREE-enriched sources. This pattern is consistent with derivation from evolved continental crust, where long-term fractionation processes have led to enrichment in light rare earth elements.

Overall, the Imiter Formation samples fall outside both the "Archean crust" and "arc rocks" fields and are clearly distinct from the MORB field, which is characterized by more positive εNd(t) values and less fractionated isotopic signatures.

The comparison with regional datasets reveals a strong isotopic similarity between the Imiter siliciclastic rocks (610–604 Ma) [23,25] and the Kerdous (583 Ma) [99] and Imiter granitoids (between 582 and 538 Ma) [49,52,54,61], suggesting that erosion of these crustal blocks provided a major part of the detrital input. The slight shift toward less negative εNd(t) values in some samples may reflect minor contributions from more juvenile sources, potentially linked to Neoproterozoic magmatic activity associated with rifting.

Overall, the Sm–Nd isotopic data indicate that the Imiter basin was predominantly fed by the erosion of the Paleoproterozoic continental crust, with only limited input from juvenile mantle-derived magmas. This interpretation is consistent with the sedimentary geochemical signatures discussed below (see Section 5.2. Tectonic Setting), which point to mixed but dominantly recycled continental sources. When integrated with the regional volcanic geochemistry indicating a rift-related setting for the Imiter Formation, the isotopic data support a model in which sedimentation occurred in an extensional basin developed on an older continental basement. In this context, syn-rift magmatism may have contributed locally to the sediment budget, but it did not dominate the isotopic signature, which remained largely controlled by erosion of the pre-existing crust.

Figure 13 illustrates the temporal evolution of εNd values for the Imiter siliciclastic samples (shales and sandstones) based on measured $^{147}Sm/^{144}Nd$ compared to the model evolution of the depleted mantle (DM) [17] and the Chondritic Uniform Reservoir (CHUR) [16]. The data define a series of linear isotopic evolution trends that project back-

ward in time toward a relatively narrow range of intersection points between the CHUR and DM curves.

The εNd values of the samples evolve with a steep slope over time due to their low $^{147}Sm/^{144}Nd$, indicating derivation from evolved crustal sources with a long-term history of light rare earth element (LREE) enrichment rather than juvenile mantle-derived material. The broadly parallel trends of the samples imply similar Sm/Nd ratios across the siliciclastic units, pointing either to a relatively homogeneous source or to well-mixed sediment inputs.

Importantly, the back-projected intersections of these trends cluster at model ages consistent with Paleoproterozoic crustal residence times. This indicates that the sediments were mainly derived from the recycling of ancient continental crust, with little contribution from contemporaneous magmatic sources. The lack of trends subparallel to the DM field further supports minimal input from juvenile mantle-derived material during sediment generation.

Some scatter among individual sample trends is present and may reflect local variations in source lithology, sediment mixing processes, or minor post-depositional modification.

However, this variability remains limited, reinforcing the interpretation of a dominant, isotopically evolved crustal provenance.

Overall, the εNd evolution patterns in Figure 13 highlight that the Imiter siliciclastics record a strong signature of crustal recycling, with provenance linked to old continental terranes. This is consistent with sedimentation in a tectonic setting where the erosion of pre-existing crustal blocks dominated over input from newly formed mantle-derived material.

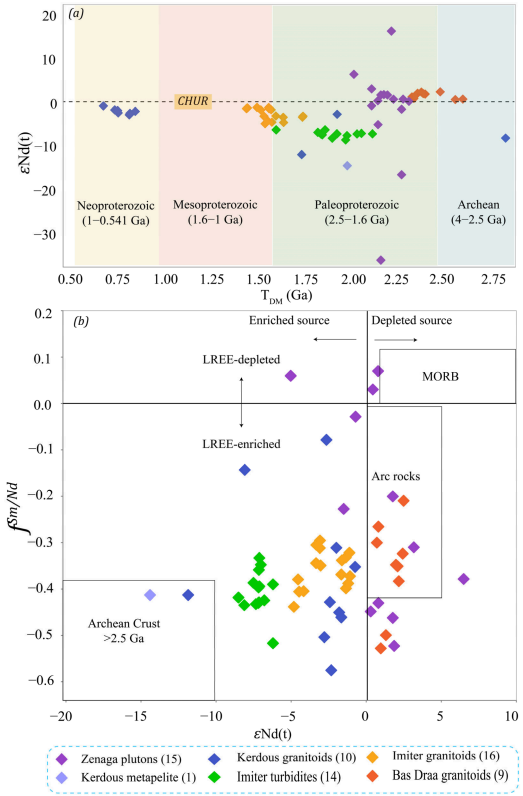


Figure 12. (**a**) Nd isotopic data εNd(t) vs. T_{DM} model age and (**b**) $f^{Sm/Nd}$ vs. εNd(t) diagram of [4] for Imiter Formation [this study; 14 samples from drill core IC954 (Imiter South)] compared with various igneous and sedimentary rock data from some Anti-Atlas Inliers, including studies by [99] (Kerdous metapelite and granitoids; 11 samples), [100] (Zenaga granitoids; 15 samples), [60] (Imiter granitoids; 16 samples), and [101] (Bas Drâa granitoids; 9 samples). $f^{Sm/Nd}$: the fractionation factor f was defined by [98]. Data for MORB and arc rocks are from [3].

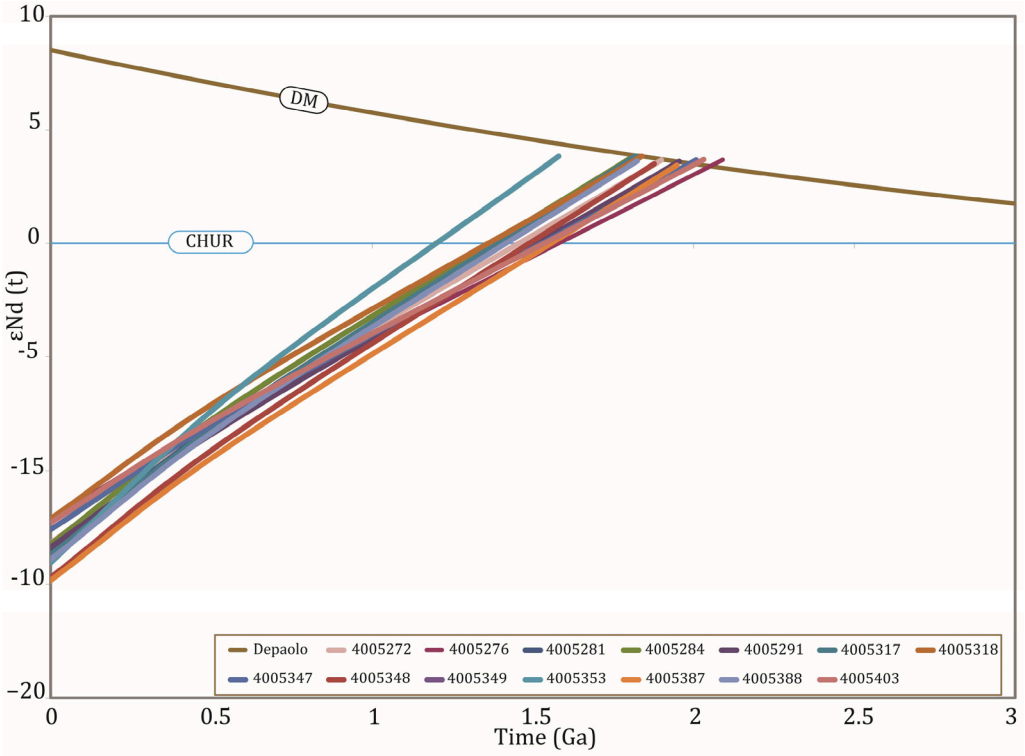


Figure 13. εNd evolution with time model for Imiter siliciclastic rocks. DM: depleted mantle after [17]; CHUR: Chondritic Uniform Reservoir after [16].

5.2. Tectonic Setting

The Saghro Group, including the Imiter Formation, comprises a folded, low-grade metamorphosed sedimentary succession reaching up to ~8 km in thickness [27,59]. The pervasive schistosity developed within the Imiter Formation reflects multiple deformation phases related to the Pan-African evolution of the Anti-Atlas, locally masking primary sedimentary features and complicating stratigraphic correlations. The succession is also intruded by mafic-to-andesitic dykes and granitoid bodies, documenting a significant post-depositional magmatic overprint. These features collectively indicate that the Imiter basin experienced a substantial tectonic and magmatic reworking during the late Neoproterozoic.

It is exposed within and north of the Pan-African suture zone in the central and eastern Anti-Atlas (Figure 1). This suture zone is delineated by the Anti-Atlas Major Fault [29] (AAMF; Figure 1), which is characterized by ophiolitic remnants and oceanic arc assemblages exposed in the Siroua and Bou Azzer inliers [31,40,41,102]. The AAMF broadly marks the northern limit of these obducted units. South of the AAMF, the Anti-Atlas inliers are interpreted as representing the deformed northern margin of the West African Craton (WAC) [32,47,100].

Within this geodynamic framework, the Saghro Group is interpreted as a Neoproterozoic deep-marine volcano–sedimentary sequence deposited in a tectonically active basin along the northern margin of the WAC [25,27,103,104]. Its evolution records a syn-tectonic basin development, most likely in a back-arc or active-margin setting, as suggested by [25] and references therein.

Previous studies constraining the tectonic setting of Precambrian basins have mainly relied on major and trace element geochemical diagrams proposed by [11,105]. However, as emphasized by [1,2], these approaches have important limitations and may not provide sufficiently robust discrimination of tectonic settings. To overcome these issues, [1,2] introduced new discrimination schemes based on discriminant functions and multidimensional diagrams, specifically designed for Precambrian sedimentary successions. The multidimen-

sional discriminant-function diagrams of [1,2], based on log-ratio transformations of major and trace element data, provide a statistically robust approach to the tectonic classification of siliciclastic sediments. These diagrams show high reliability and are particularly well suited for Precambrian rocks, as they are relatively resistant to the effects of weathering, sediment recycling, and low-grade metamorphism. However, their interpretation should be supported by sedimentological and structural evidence, because bulk-rock composition can still be influenced by both provenance and recycling processes.

In the major element discrimination diagrams (Figure 14a,b), the high-silica samples (SiO_2 = 63–95 wt.% sandstones) of the Imiter Formation plot mainly within the continental rift and arc fields, with only minor extension toward the collision domain. This pattern suggests derivation from tectonically active settings, such as intracontinental rifts and/or magmatic arc environments. By contrast, the low-silica samples (SiO_2 = 35–63 wt.% shales) plot predominantly within the continental rift field but show a wider spread into the arc and collision domains. This broader distribution likely reflects mixed sediment sources and a higher degree of sediment homogenization.

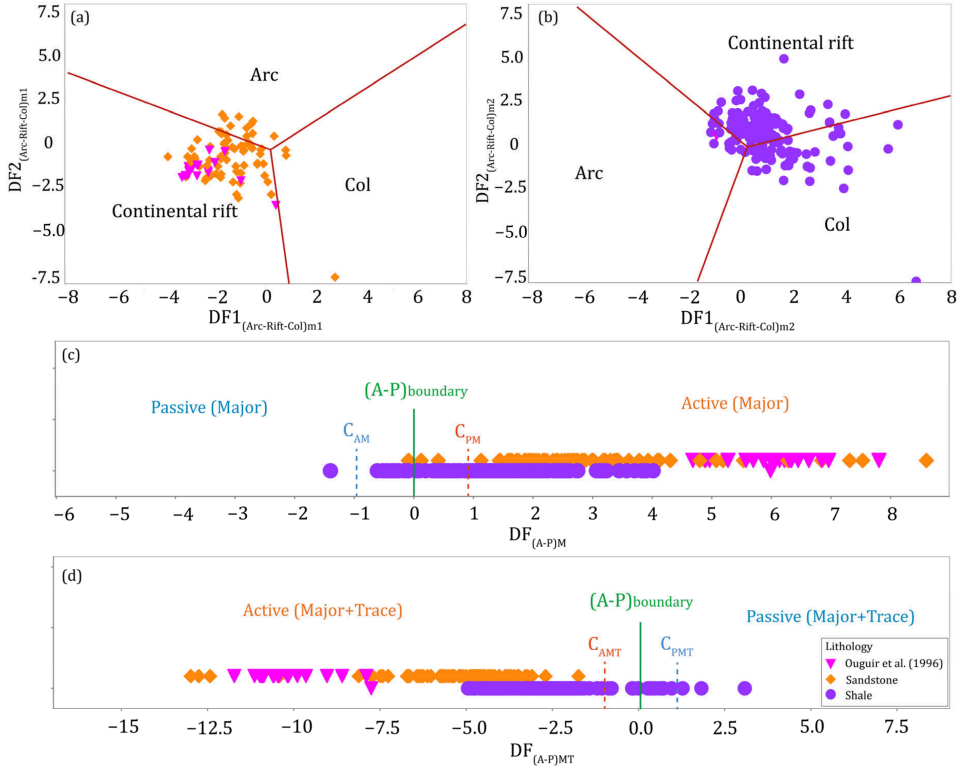


Figure 14. Tectonic discrimination diagrams [1,2] applied to the shales and sandstones of Imiter Formation: (**a**) Major element-based discrimination diagram: $DF2_{(Arc\text{-}Rift\text{-}Col)m1}$ versus $DF1_{(Arc\text{-}Rift\text{-}Col)m1}$ for high-silica samples (SiO_2 = 63–95 wt.%); (**b**) major element-based discrimination diagram: $DF2_{(Arc\text{-}Rift\text{-}Col)m2}$ versus $DF1_{(Arc\text{-}Rift\text{-}Col)m2}$ for low-silica samples (SiO_2 = 35–63 wt.%); (**c**) major element-based discrimination $DF_{(A\text{-}P)\,M}$ diagram; and (**d**) combined major and trace element discrimination $DF_{(A\text{-}P)\,MT}$ diagram. Literature data were taken from [27]. Abbreviations: Col = collision; A = active margin; P = passive margin; A-P Boundary = active–passive margins boundary; C_{AM} = centroid of active margin for major elements; C_{PM} = centroid of passive margin for major elements; C_{AMT} = centroid of active margin for major and trace elements; C_{PMT} = centroid of passive margin for major and trace elements. The functions (DF) were calculated based on the following equations of [1,2].

The $DF_{(A–P)\,M}$ diagram (Figure 14c), based on major elements, clearly distinguishes between passive and active tectonic settings. The sandstones of the Imiter Formation predominantly plot within the active field, with relatively high positive values consistent with

an active-margin affinity. By contrast, the shales show a broader distribution, with many samples falling within the passive field and others clustering near or crossing the active–passive boundary. This pattern suggests a shift toward more stable tectonic conditions and an increased influence of crustal recycling.

The combined major and trace element $DF_{(A–P)\,MT}$ diagram (Figure 14d) further reinforces this interpretation. The sandstone samples plot almost exclusively within the active field, with strongly negative values indicative of a clear active-margin signature. By contrast, the shale samples are more widely dispersed, extending from the active domain into the passive field, with several samples lying near or beyond the boundary between the two settings. This distribution reflects a stronger contribution from mature, recycled continental sources.

Importantly, these sedimentary geochemical signatures are consistent with the regional magmatic record. The geochemistry of mafic volcanic rocks (basalts) associated with the Saghro Group in surrounding inliers of the Imiter Sub-inlier—particularly the Boumalne Dades and Qalât Mgouna Sub-inliers, as well as in the Siroua massif (Figures 1 and 2)—indicates affinities with initial rift tholeiites, continental tholeiites, and oceanic island alkali basalts [21,104,106]. These volcanic signatures strongly support the development of a continental rift environment.

The convergence of sedimentary and volcanic geochemical evidence, therefore, reinforces the interpretation that the Imiter basin evolved within an extensional tectonic regime. The predominance of active-margin signatures in the sandstones likely reflects input from syn-rift magmatism and tectonically active source areas, whereas the more dispersed and passive signatures recorded in the shales point to progressive basin stabilization, increased sediment recycling, and greater contribution from mature continental crust.

$$DF1_{(Arc\text{-}Rift\text{-}Col)m1} = (-0.263 \times In[TiO_2/SiO_2]_{adj}) + (0.604 \times In[Al_2O_3/SiO_2]_{adj}) + (-1.725 \times In[Fe_2O_3{}^t/SiO_2]_{adj}) + (0.660 \times In[MnO/SiO_2]_{adj}) + (2.191 \times In[MgO/SiO_2]_{adj}) + (0.144 \times In[CaO/SiO_2]_{adj}) + (-1.304 \times In[Na_2O/SiO_2]_{adj}) + (0.054 \times In[K_2O/SiO_2]_{adj}) + (-0.330 \times In[P_2O_5/SiO_2]_{adj}) + 1.588.$$

$$DF2_{(Arc\text{-}Rift\text{-}Col)m1} = (-1.196 \times In[TiO_2/SiO_2]_{adj}) + (1.604 \times In[Al_2O_3/SiO_2]_{adj}) + (0.303 \times In[Fe_2O_3{}^t/SiO_2]_{adj}) + (0.436 \times In[MnO/SiO_2]_{adj}) + (0.838 \times In[MgO/SiO_2]_{adj}) + (-0.407 \times In[CaO/SiO_2]_{adj}) + (1.021 \times In[Na_2O/SiO_2]_{adj}) + (-1.706 \times In[K_2O/SiO_2]_{adj}) + (-0.126 \times In[P_2O_5/SiO_2]_{adj}) - 1.068.$$

$$DF1_{(Arc\text{-}Rift\text{-}Col)m2} = (0.608 \times In(TiO_2/SiO_2)_{adj}) + (-1.854 \times In(Al_2O_3/SiO_2)_{adj}) + (0.299 \times In(Fe_2O_3{}^t/SiO_2)_{adj}) + (-0.550 \times In(MnO/SiO_2)_{adj}) + (0.120 \times In(MgO/SiO_2)_{adj}) + (0.194 \times In(CaO/SiO_2)_{adj}) + (-1.510 \times In(Na_2O/SiO_2)_{adj}) + (1.941 \times In(K_2O/SiO_2)_{adj}) + (0.003 \times In(P_2O_5/SiO_2)_{adj}) - 0.294.$$

$$DF2_{(Arc\text{-}Rift\text{-}Col)m2} = (-0.554 \times In(TiO_2/SiO_2)_{adj}) + (-0.995 \times In(Al_2O_3/SiO_2)_{adj}) + (1.765 \times In(Fe_2O_3{}^t/SiO_2)_{adj}) + (-1.391 \times In(MnO/SiO_2)_{adj}) + (-1.034 \times In(MgO/SiO_2)_{adj}) + (0.225 \times In(CaO/SiO_2)_{adj}) + (0.713 \times In(Na_2O/SiO_2)_{adj}) + (0.330 \times In(K_2O/SiO_2)_{adj}) + (0.637 \times In(P_2O_5/SiO_2)_{adj}) - 3.631.$$

$$DF_{(AP)M} = (3.0005 \times ilr1_{TiM}) + (-2.8243 \times ilr2_{AlM}) + (-1.0596 \times ilr3_{FeM}) + (-0.7056 \times ilr4_{MnM}) + (-0.3044 \times ilr5_{MgM}) + (0.6277 \times ilr6_{CaM}) + (-1.1838 \times ilr7_{NaM}) + (1.5915 \times ilr8_{KM}) + (0.1526 \times ilr9_{PM}) - 5.9948.$$

$$DF_{(AP)\,MT} = (3.2683 \times ilr1_{TiMT}) + (5.3873 \times ilr2_{AlMT}) + (1.5546 \times ilr3_{FeMT}) + (3.2166 \times ilr4_{MnMT}) + (4.7542 \times ilr5_{MgMT}) + (2.0390 \times ilr6_{CaMT}) + (4.0490 \times ilr7_{NaMT}) + (3.1505 \times ilr8_{KMT}) + (2.3688 \times ilr9_{PMT}) + (2.8354 \times ilr10_{CrMT}) + (0.9011 \times ilr11_{NbMT}) + (1.9128 \times ilr12_{NiMT}) + (2.9094 \times ilr13_{VMT}) + (4.1507 \times ilr14_{YMT}) + (3.4871 \times ilr15_{ZrMT}) - 3.2088.$$

5.3. Sedimentary Paleoenvironment

5.3.1. Paleoclimate, Chemical Weathering and Depositional Environment

Paleoclimate exerts a primary control on the mineralogy and chemical composition of detrital material forming clastic sediments [107]. Major element abundances (Al_2O_3, Na_2O, K_2O) and weathering indices such as CIA, CIW, PIA, and ICV are widely used to evaluate the intensity of chemical weathering and, consequently, paleoclimatic conditions, whereas trace elements provide complementary constraints on depositional environments.

In contrast, SiO_2 in sandstones primarily reflects quartz content and sediment maturity rather than acting as a direct paleoclimate proxy.

The integrated geochemical proxies displayed in Figure 15 provide coherent constraints on weathering intensity, sediment compositional maturity, paleoclimatic conditions, and depositional setting of the Imiter Formation.

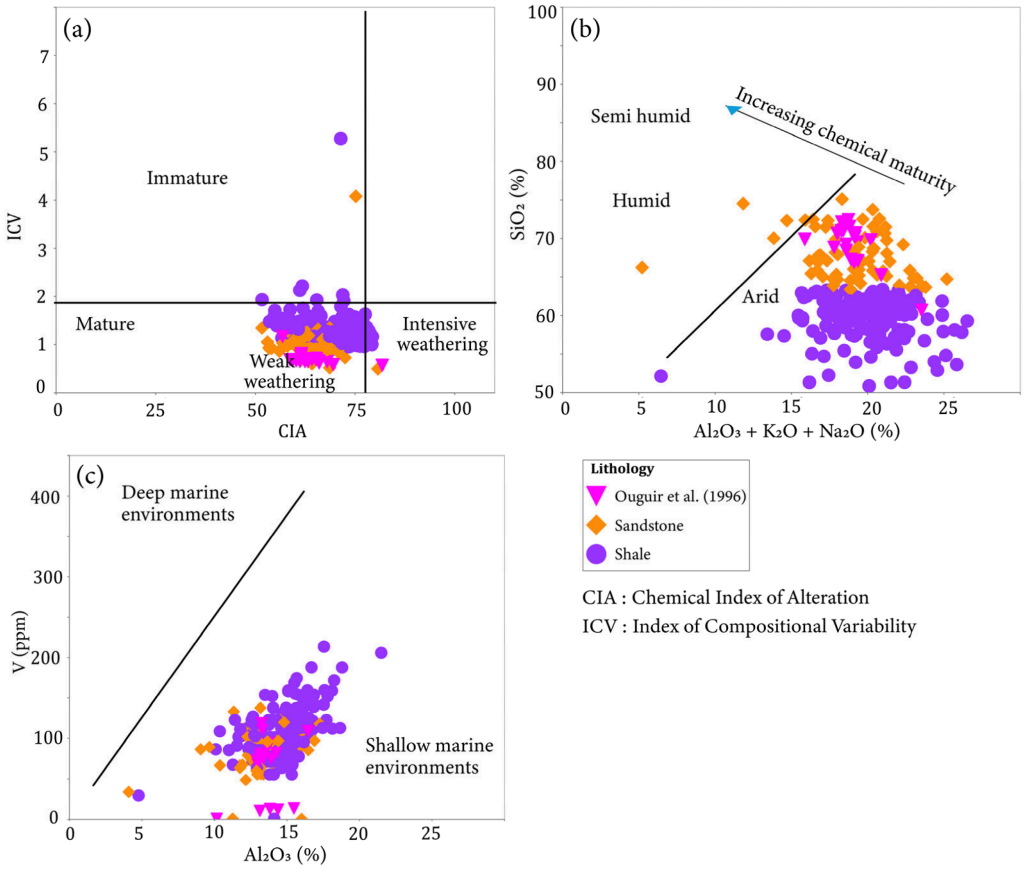


Figure 15. Graphs illustrating (**a**) ICV versus CIA bivariate diagram according to [4]; (**b**) Al_2O_3 + K_2O + Na_2O (wt.%) versus SiO_2 (wt.%) bivariate diagram from [108] and (**c**) V (ppm) versus Al_2O_3 (wt.%) bivariate diagram from [109]. Literature data were taken from [27].

In the bivariate Index of Compositional Variability (ICV) versus Chemical Index of Alteration (CIA) diagram [4] (Figure 15a), most samples cluster around CIA values of ~60–75 and ICV values generally below 2. This pattern reflects weak-to-moderate chemical weathering combined with a relatively mature sediment composition. The predominance of ICV values <1.5 points to enrichment in clay minerals and depletion in unstable components, consistent with sediment recycling and/or prolonged weathering [12,75]. However, the absence of very high CIA values (>80) suggests that extreme chemical leaching under strongly humid tropical conditions was unlikely. Overall, the data trend falls mainly within the "weak to moderate weathering" field, with only limited extension into the "intense

weathering" domain, indicating intermediate weathering conditions in the source areas, likely controlled by fluctuating climate rather than persistently humid conditions.

This interpretation is supported by CIA values ranging from 53.9 to 75.5 (average 65.2), as well as CIW (57–89.2; average 76.62) and PIA (64.7–87.3; average 72.8), which collectively point to moderate feldspar alteration and incomplete weathering of plagioclase [76,77].

The relationship between CIA and ICV (Figure 15a), together with the relative enrichment in Al_2O_3, K_2O, and Na_2O, further supports limited-to-moderate chemical weathering of the parent rocks.

The SiO_2 versus (Al_2O_3 + K_2O + Na_2O) diagram [108] (Figure 15b) further refines this interpretation. Most samples plot within the arid climatic field. The sandstones are characterized by relatively higher SiO_2 contents and slightly lower concentrations of feldspar-related oxides, reflecting quartz enrichment through sedimentary reworking and/or progressive feldspar breakdown during weathering. In contrast, the shales show comparatively higher Al_2O_3 + alkali contents, consistent with a greater abundance of clay minerals.

Overall, this distribution suggests that chemical weathering was sufficient to induce partial feldspar alteration, but not intense enough to completely remove mobile cations. The inferred paleoclimate is therefore best described as arid, with episodic weathering and sediment input rather than sustained intense chemical alteration.

Mineralogical observations further support this interpretation. The presence of plagioclase, K-feldspar, and mica in thin sections (Figure 6) indicates limited chemical alteration and is consistent with relatively low weathering intensity under arid conditions [107]. This assemblage suggests that the source rocks experienced only moderate alteration, allowing the sediments to retain a composition dominated by relatively resistant primary minerals.

The V versus Al_2O_3 relationships [109] (Figure 15c) provide further constraints on depositional redox conditions and basin setting. The positive correlation between V and Al_2O_3 reflects the association of vanadium with clay minerals and fine-grained fractions, indicating that V is mainly hosted in detrital or adsorbed phases rather than resulting from authigenic enrichment under strongly reducing conditions [109].

Most samples plot within the shallow marine field. Vanadium (V) concentrations are generally moderate, with most values below 200 ppm. The studied samples display variable V contents, with no evidence of significant enrichment.

Taken together, these geochemical and mineralogical data point to a coherent paleoenvironmental model characterized by: (i) source areas affected by weak-to-moderate chemical weathering, (ii) sediments of mixed compositional maturity reflecting both primary detrital input and secondary recycling, (iii) deposition under generally arid climatic conditions, and (iv) accumulation within a shallow marine basin under predominantly oxic-to-mildly reducing conditions.

This integrated interpretation is consistent with the sedimentological features of the Imiter Formation, which indicate shallow marine to turbiditic depositional environments influenced by variable sediment supply and climatic controls [27,56].

5.3.2. Redox Conditions and Organic Carbon Dynamics

The V–Ni systematics [80] provide important constraints on the redox structure of the Imiter Basin (Figure 16). Most samples define a consistent positive V–Ni trend within the marine–terrestrial oxic–dysoxic field, suggesting deposition under persistently oxygen-limited but not fully anoxic conditions. This is further supported by generally low V/Ni ratios (<3), indicating that the basin did not experience long-lasting euxinic conditions, but rather fluctuated under suboxic conditions typical of shallow, weakly stratified environments.

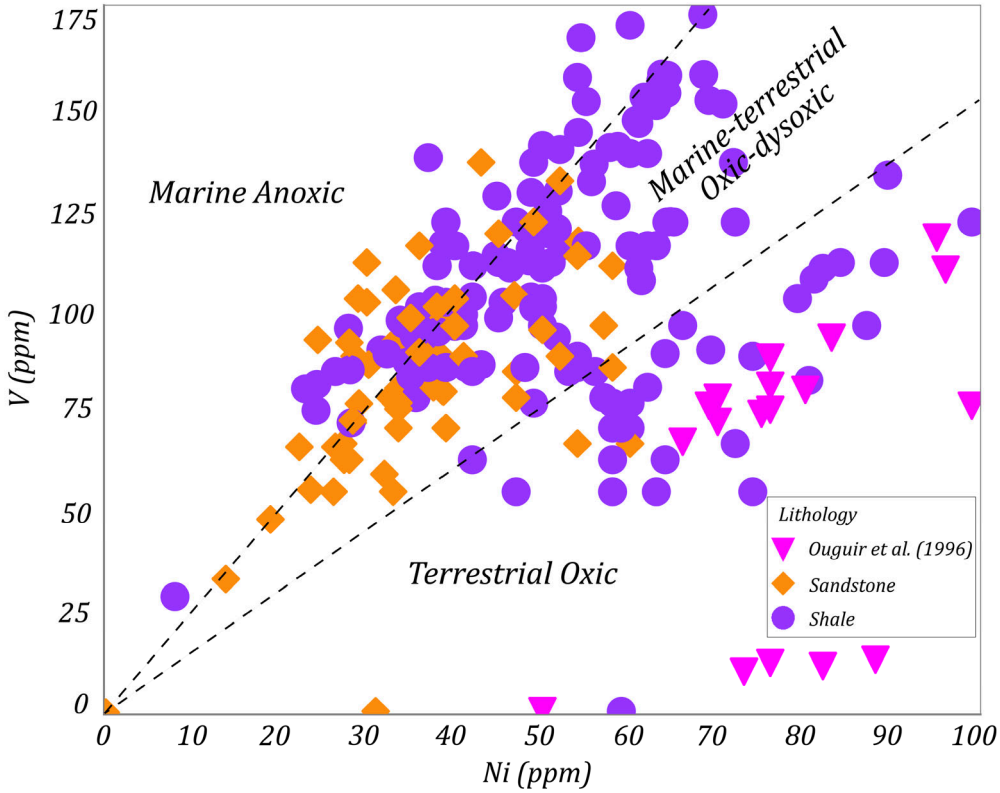


Figure 16. Determination of paleo-redox conditions (oxic–dysoxic–anoxic) based on the Ni (ppm) versus V (ppm) diagram of shales and sandstones from the Imiter Formation of Saghro Group. The discrimination fields are after [80,82]. Literature data compiled from [27] are included for comparison.

Occasional shifts of both shale and sandstone samples into the marine anoxic field likely reflect short-lived episodes of enhanced vanadium enrichment and improved organic matter preservation, pointing to transient redox intensification rather than sustained basin-wide anoxia. The convergence of these data with elevated V/(V + Cr) and V/(V + Ni) ratios (see Figure S1a–d in the Supplementary Materials) confirms that reducing conditions were episodic and spatially restricted, likely linked to transient water-column stratification or productivity pulses. High V/(V + Cr) and V/(V + Ni) ratios are widely used to infer depositional redox conditions, with values > 0.6 and >0.8, respectively, generally considered indicative of reducing environments [81,83]. In the studied succession, V/(V + Cr) exceeds 0.6 in several shale samples and approaches this threshold in sandstone-dominated intervals. Similarly, V/(V + Ni) values commonly exceed 0.8 in shales and remain close to this threshold in sandstones, suggesting the occurrence of localized or intermittent reducing conditions. However, these proxies must be interpreted in conjunction with other redox indicators. The generally low V/Ni ratios (<3) and the distribution of samples in the V–Ni discrimination diagram indicate that deposition occurred predominantly under oxic-to-dysoxic conditions [80]. Taken together, these results suggest short-lived reducing episodes superimposed on an overall well-oxygenated depositional environment.

Conversely, shale and sandstone samples, including those from the literature data of [27], that plot within the terrestrial oxic field record well-oxygenated, high-energy depositional environments. This supports a strong proximal continental influence and efficient sediment reworking, while their geochemical dilution patterns highlight the limited potential for trace-metal enrichment in higher-energy settings.

Overall, the V–Ni distribution reveals a dynamic redox mosaic in which oxic, dysoxic, and locally anoxic conditions coexisted within a laterally variable depositional system. This heterogeneity is best explained by a shallow marine–continental transitional basin,

characterized by rapid changes in accommodation space, clastic input, and water-column ventilation, rather than a stable, persistently reducing environment.

The strong agreement between V–Ni systematics and independent redox proxies (Ni/Co, V/Cr, V/Ni, V/(V + Ni), and V/(V + Cr)) indicates that the Imiter Formation records a redox-unstable depositional setting, where oxygen limitation was frequent but rarely extreme. Local geochemical perturbations near mafic and andesitic intrusions may reflect secondary remobilization processes, but they do not significantly alter the primary basin-scale signal.

Overall, Figure 16 depicts a system controlled by short-lived redox fluctuations, where organic matter preservation and trace-metal enrichment were mainly governed by transient episodes of reducing conditions within an overall oxic-to-dysoxic basin during the lower Ediacaran.

Despite being described as "black shales" in previous studies [27], the analyzed shale and sandstone samples contain uniformly low TOC content (0.1–0.3 wt.%), well below the threshold commonly used to define true black shales (>0.5 wt.% TOC) [110,111]. Organic-rich black shales typically contain several weight percent TOC and may exceed 10 wt.% in exceptionally enriched deposits. The consistently low organic carbon content, therefore, indicates that the Imiter shales are more appropriately classified as organic-lean shales rather than true black shales, which suggests that conditions favorable for long-term organic matter accumulation and preservation were not sustained during deposition.

The $\delta^{13}C_{org}$ values range from −27.7‰ to −25.6‰ VPDB (Table S4 and Figure S1a, Supplementary Material), falling within the range commonly reported for Ediacaran marine organic matter. Such values are generally consistent with organic carbon derived predominantly from marine photoautotrophic biomass fixed through oxygenic photosynthesis. The relatively restricted isotopic range suggests limited variability in the dominant organic matter source and/or in the isotopic composition of the dissolved inorganic carbon reservoir during deposition.

Taken together, the low TOC content and relatively uniform $\delta^{13}C_{org}$ values indicate limited organic carbon accumulation throughout the depositional history of the Imiter Formation. Combined with redox-sensitive trace element proxies, these data suggest that organic matter preservation was restricted under predominantly oxic-to-dysoxic conditions, although variations in primary productivity cannot be excluded. Consequently, the studied succession differs markedly from typical organic-rich black shale systems that develop under persistent anoxic-to-euxinic conditions favorable for enhanced carbon burial.

This interpretation is consistent with the redox-sensitive trace element systematics discussed above. The predominance of low V/(V + Ni) and V/Cr ratios, together with generally low TOC content, indicates that oxygenated bottom waters were common during deposition. Although some samples record temporary shifts toward more reducing conditions, these episodes were insufficient to promote significant organic matter preservation. Overall, organic carbon accumulation in the Imiter Basin appears to have been controlled primarily by preservation efficiency under fluctuating redox conditions rather than by exceptional organic productivity.

5.3.3. Comparison with Ediacaran Carbon Isotope Records and Implications for Carbon Cycling

The Ediacaran Period was characterized by pronounced fluctuations in the global carbon cycle reflected by large variations in both carbonate and organic carbon isotope records [112–114]. These isotopic excursions have been linked to major environmental and biogeochemical changes associated with the aftermath of Cryogenian glaciations, evolving ocean redox conditions, enhanced nutrient cycling, and the diversification of early complex ecosystems [115].

Against this backdrop, the organic carbon isotopic composition of the Imiter Formation shales is characterized by a relatively narrow range of $\delta^{13}C_{org}$ values (−27‰ to −25‰), contrasting with the broader and more dynamic isotopic variability reported from Ediacaran successions such as the Wangji drill core on the Yangtze Platform, South China [116]. There, $\delta^{13}C_{org}$ values range from −22‰ to −34‰ and exhibit large amplitude excursions that closely track variations in $\delta^{13}C_{carb}$. This coupled behavior has been interpreted as evidence of major perturbations in the oceanic carbon cycle, driven by episodic upwelling and the incorporation of ^{13}C-depleted dissolved organic carbon from deep waters. Such conditions are commonly associated with enhanced primary productivity, sustained nutrient supply, and phosphogenic depositional environments [116].

By contrast, the carbon isotope record of the Imiter Formation does not display the pronounced excursions observed in some Ediacaran successions. Instead, $\delta^{13}C_{org}$ values remain relatively stable despite variations in TOC content and redox-sensitive trace element proxies. This decoupling between isotopic composition and organic carbon abundance suggests that fluctuations in TOC were controlled primarily by preservation efficiency under changing redox conditions rather than by major shifts in the isotopic composition of the carbon source.

The relatively restricted range of $\delta^{13}C_{org}$ values observed in the analyzed samples contrasts with the large-amplitude isotopic excursions reported from several Ediacaran basins worldwide. However, because the present dataset does not represent a continuous stratigraphic record, it does not allow evaluation of temporal isotopic excursions within the Imiter Formation. Nevertheless, the relatively uniform $\delta^{13}C_{org}$ values obtained from the analyzed samples are consistent with a predominantly marine organic matter source and suggest limited variability in the isotopic composition of the dissolved inorganic carbon reservoir during deposition.

Overall, this comparison highlights a key difference between the Imiter Basin and the phosphogenic Ediacaran basins of South China. Whereas the latter record significant carbon cycle instability linked to intensified nutrient cycling and recurrent upwelling, the Imiter Formation preserves a comparatively stable organic carbon isotope signal dominated by local depositional and preservation controls. This distinction emphasizes the important role of basin setting in regulating how global biogeochemical changes are recorded in the sedimentary archive.

6. Conclusions

The integrated petrographic, whole-rock geochemical, Sm–Nd isotopic, and organic geochemical dataset provides new constraints on the provenance, depositional conditions, and tectono-sedimentary evolution of the Ediacaran Imiter Formation in the eastern Anti-Atlas.

Major and trace element compositions, together with REE systematics, indicate that the siliciclastic succession was derived predominantly from felsic-to-intermediate upper continental crust sources. Immobile trace element ratios (e.g., Th/Sc, La/Sc, and Zr/Sc) show limited compositional variability and only minor evidence of zircon enrichment, suggesting that source rock composition exerted a stronger control on sediment chemistry than sediment recycling processes. Sm–Nd isotopic signatures further support this interpretation, with consistently negative εNd(t) values (−8.5 to −6.2) and Paleoproterozoic model ages (~1.6–2.1 Ga) indicating that derivation mainly from evolved crustal domains related to the West African Craton and its Pan-African reworking.

Weathering indices (CIA, CIW, and PIA), supported by petrographic observations, indicate weak-to-moderate chemical weathering in the source areas. The preservation of feldspar and mica suggests limited alteration under predominantly arid climatic condi-

tions, which resulted in the incomplete chemical breakdown of primary minerals prior to deposition.

Redox-sensitive trace element proxies indicate predominantly oxic-to-dysoxic depositional conditions punctuated by localized episodes of reduced oxygenation. Organic geochemical data reveal uniformly low TOC content (0.1–0.3 wt.%) and $\delta^{13}C_{org}$ values ranging from −27.7‰ to −25.6‰, consistent with predominantly marine photoautotrophic organic matter. These characteristics indicate limited organic matter preservation and confirm that the studied shales are organic-lean rather than true black shales.

The combined geochemical and isotopic evidence supports deposition within a syn-orogenic-to-post-orogenic extensional basin developed during the late Pan-African evolution of the Anti-Atlas. The Imiter Basin records sedimentation in an active-margin geodynamic framework displaying characteristics transitional between back-arc and intracontinental extensional settings. Sediment supply was dominated by the erosion of Pan-African arc-related rocks and an older continental basement, with only a minor contribution from mafic sources.

Overall, the Imiter Formation preserves the record of a shallow marine siliciclastic basin fed mainly by recycled Paleoproterozoic continental crust, affected by moderate weathering and deposited under predominantly oxygenated conditions during the Ediacaran evolution of the northern Gondwana margin. These results contribute to refining the paleogeographic and geodynamic reconstruction of the Anti-Atlas and provide new insights into the sedimentary processes operating during the late stages of the Pan-African tectonic evolution.

Supplementary Materials: The following supporting information can be downloaded at: https://www.mdpi.com/article/10.3390/geosciences16070288/s1, Table S1 Supplementary Material. Major and trace element compositions of shales and sandstones from the Imiter Formation, analyzed from three boreholes: SFC2904 (Imiter West; n = 63), IC732 (Imiter Center; n = 47), and SFC2877 (Imiter East; n = 139). Comparative data for surface samples are sourced from [27]. Analytical standards and procedures were provided by the Research, Mining and Exploration Centre (REMINEX), Managem Group (Morocco). Table S2 Supplementary Material. Major, trace and rare earth elements (REEs) element compositions of shales and sandstones from the Imiter Formation, analyzed from the borehole: IC954 (Imiter South; n = 14). Analytical standards, precision and procedures were provided by Analytical Laboratory Services (ALS) Global Laboratories (North Vancouver, Canada), in collaboration with Carleton University. Table S3 Supplementary Material. Sm-Nd isotopic compositions of shales and sandstones from the Imiter Formation, analyzed from the borehole: IC954 (Imiter South; n = 14). Analytical standards and procedures were provided by Analytical Laboratory Services (ALS) Global Laboratories (North Vancouver, Canada), in collaboration with Carleton University. εNd (t) values were calculated at t = 604 Ma. Table S4 Supplementary Material. Total organic carbon (TOC) and organic carbon isotope ($\delta^{13}C_{org}$) compositions of shales and sandstones from the Imiter Formation, analyzed from the borehole: IC954 (Imiter South; n = 14). Analytical standards and procedures were provided by Andrey Bekker Lab at the Department of Earth and Planetary Sciences, University of California, Riverside (USA). Figure S1 Supplementary Material. (a) Profiles of organic carbon isotope ($\delta^{13}C_{org}$), total organic carbon (TOC), redox proxies, and sediment proxies provenance for shales and sandstones from the Imiter Formation from the borehole: IC954 (Imiter South). (b) Profiles of paleoweathering–paleoclimate and redox proxies for shales and sandstones from the Imiter Formation from the borehole SFC2877 (Imiter East). (c) Profiles of paleoweathering–paleoclimate and redox proxies for shales and sandstones from the Imiter Formation from the borehole IC732 (Imiter Centre). (d) Profiles of paleoweathering–paleoclimate and redox proxies for shales and sandstones from the Imiter Formation from the borehole: SFC2904 (Imiter West).

Author Contributions: Conceptualization, M.H. and N.Y.; methodology, M.H.; software, M.H.; validation, N.Y., A.S., B.C., L.M., M.Z., L.R. and M.A.B.; formal analysis, M.H.; data curation, M.H.; writing—original draft preparation, M.H. and N.Y.; writing—review and editing, M.H., N.Y., B.C., A.S., E.H.C., H.O., H.H. Y.A. and L.R.; visualization, M.H.; supervision, M.H., N.Y., A.S. and E.H.C.; project administration, M.H. All authors have read and agreed to the published version of the manuscript.

Funding: This research received no external funding.

Data Availability Statement: All data generated or analyzed during this study are included in this published article and its Supplementary Materials.

Acknowledgments: This work forms part of Mohamed Hamouyahia's doctoral dissertation, conducted under the supervision of Nasrrddine Youbi, to be submitted to the Department of Geology, Faculty of Sciences Semlalia, Cadi Ayyad University of Marrakech. It is the result of a collaboration between the Department of Geology, Faculty of Sciences Semlalia, Cadi Ayyad University of Marrakech; the Department of Earth Sciences, Carleton University, Ottawa, Canada; the Department of Earth and Planetary Sciences, University of California, Riverside, USA; and the Managem Group. We sincerely thank the anonymous reviewers for their constructive comments and suggestions, which significantly improved the manuscript.

Conflicts of Interest: Authors Mohamed Hamouyahia, Lhou Maacha, Mohamed Zouhair and Lahcen Rakhiss were employed by Managem Group, which had no input in the research processes or results presented. All other authors declare no conflicts of interest.

References

1. Verma, S.P.; Armstrong-Altrin, J.S. New Multi-Dimensional Diagrams for Tectonic Discrimination of Siliciclastic Sediments and Their Application to Precambrian Basins. *Chem. Geol.* **2013**, *355*, 117–133. [CrossRef]
2. Verma, S.P.; Armstrong-Altrin, J.S. Geochemical Discrimination of Siliciclastic Sediments from Active and Passive Margin Settings. *Sediment. Geol.* **2016**, *332*, 1–12. [CrossRef]
3. Yardley, B.W.D. The Continental Crust: Its Composition and Evolution by S. R. Taylor and S. M. McClennan, Blackwell Scientific Publications, Oxford, 1985. No. of Pages: 312 + XV Pp. Price: £16.80 (Soft Covers). *Geol. J.* **1986**, *21*, 85–86. [CrossRef]
4. McLennan, S.M.; Hemming, S.; McDaniel, D.K.; Hanson, G.N. Geochemical Approaches to Sedimentation, Provenance, and Tectonics. In *Geological Society of America Special Papers*; Geological Society of America: Boulder, CO, USA, 1993; Vol. 284, pp. 21–40. ISBN 978-0-8137-2284-9.
5. Bakkiaraj, D.; Nagendra, R.; Nagarajan, R.; Armstrong-Altrin, J.S. Geochemistry of Sandstones from the Upper Cretaceous Sillakkudi Formation, Cauvery Basin, Southern India: Implication for Provenance. *J. Geol. Soc. India* **2010**, *76*, 453–467. [CrossRef]
6. Armstrong-Altrin, J.S.; Nagarajan, R.; Lee, Y.I.; Kasper-Zubillaga, J.J.; Córdoba-Saldaña, L.P. Geochemistry of Sands along the San Nicolás and San Carlos Beaches, Gulf of California, Mexico: Implications for Provenance and Tectonic Setting. *Turk. J. Earth Sci.* **2014**, *23*, 533–558. [CrossRef]
7. Garzanti, E.; Resentini, A. Provenance Control on Chemical Indices of Weathering (Taiwan River Sands). *Sediment. Geol.* **2016**, *336*, 81–95. [CrossRef]
8. Armstrong-Altrin, J.S. Detrital Zircon U–Pb Geochronology and Geochemistry of the Riachuelos and Palma Sola Beach Sediments, Veracruz State, Gulf of Mexico: A New Insight on Palaeoenvironment. *J. Palaeogeogr.* **2020**, *9*, 28. [CrossRef]
9. Armstrong-Altrin, J.S.; Madhavaraju, J.; Vega-Bautista, F.; Ramos-Vázquez, M.A.; Pérez-Alvarado, B.Y.; Kasper-Zubillaga, J.J.; Ekoa Bessa, A.Z. Mineralogy and Geochemistry of Tecolutla and Coatzacoalcos Beach Sediments, SW Gulf of Mexico. *Appl. Geochem.* **2021**, *134*, 105103. [CrossRef]
10. Armstrong-Altrin, J.S.; Ramos-Vázquez, M.A.; Hermenegildo-Ruiz, N.Y.; Madhavaraju, J. Microtexture and U–Pb Geochronology of Detrital Zircon Grains in the Chachalacas Beach, Veracruz State, Gulf of Mexico. *Geol. J.* **2021**, *56*, 2418–2438. [CrossRef]
11. Bhatia, M.R.; Crook, K.A.W. Trace Element Characteristics of Graywackes and Tectonic Setting Discrimination of Sedimentary Basins. *Contr. Mineral. Petrol.* **1986**, *92*, 181–193. [CrossRef]
12. Cullers, R. Geochemistry of the Mesoproterozoic Lakhanda Shales in Southeastern Yakutia, Russia: Implications for Mineralogical and Provenance Control, and Recycling. *Precambrian Res.* **2000**, *104*, 77–93. [CrossRef]
13. Nesbitt, H.W.; Young, G.M. Early Proterozoic Climates and Plate Motions Inferred from Major Element Chemistry of Lutites. *Nature* **1982**, *299*, 715–717. [CrossRef]

14. Dar, S.A.; Khan, K.F.; Mir, A.R. Provenance and Paleo-Weathering of Paleoproterozoic Siliciclastic Sedimentary Rocks of Bijawar Group, Sonrai Basin, Uttar Pradesh, India: Using a Geochemical Approach. *J. Sediment. Environ.* **2020**, *5*, 399–413. [CrossRef]
15. Ekoa Bessa, A.Z.; Ndjigui, P.-D.; Fuh, G.C.; Armstrong-Altrin, J.S.; Betsi, T.B. Mineralogy and Geochemistry of the Ossa Lake Complex Sediments, Southern Cameroon: Implications for Paleoweathering and Provenance. *Arab J. Geosci.* **2021**, *14*, 322. [CrossRef]
16. Jacobsen, S.B.; Wasserburg, G.J. Sm-Nd Isotopic Evolution of Chondrites. *Earth Planet. Sci. Lett.* **1980**, *50*, 139–155. [CrossRef]
17. DePaolo, D.J. Neodymium Isotopes in the Colorado Front Range and Crust–Mantle Evolution in the Proterozoic. *Nature* **1981**, *291*, 193–196. [CrossRef]
18. Goldstein, S.L.; O'Nions, R.K.; Hamilton, P.J. A Sm-Nd Isotopic Study of Atmospheric Dusts and Particulates from Major River Systems. *Earth Planet. Sci. Lett.* **1984**, *70*, 221–236. [CrossRef]
19. Gromet, L.P.; Haskin, L.A.; Korotev, R.L.; Dymek, R.F. The "North American Shale Composite": Its Compilation, Major and Trace Element Characteristics. *Geochim. Et. Cosmochim. Acta* **1984**, *48*, 2469–2482. [CrossRef]
20. Rudnick, R.L.; Gao, S. Composition of the Continental Crust. In *Treatise on Geochemistry*; Elsevier, 2003; pp. 1–64. ISBN 978-0-08-043751-4.
21. Thomas, R.J.; Chevallier, L.P.; Gresse, P.G.; Harmer, R.E.; Eglington, B.M.; Armstrong, R.A.; De Beer, C.H.; Martini, J.E.J.; De Kock, G.S.; Macey, P.H.; et al. Precambrian Evolution of the Sirwa Window, Anti-Atlas Orogen, Morocco. *Precambrian Res.* **2002**, *118*, 1–57. [CrossRef]
22. Thomas, R.J.; Fekkak, A.; Ennih, N.; Errami, E.; Loughlin, S.C.; Gresse, P.G.; Chevallier, L.P.; Liégeois, J.-P. A New Lithostratigraphic Framework for the Anti-Atlas Orogen, Morocco. *J. Afr. Earth Sci.* **2004**, *39*, 217–226. [CrossRef]
23. Liégeois, J.-P. The Lower Ediacaran (630–610 Ma) Saghro Group: An Orogenic Transgressive Basin Development during the Early Metacratonic Evolution of the Anti-Atlas (Morocco). In Proceedings of the IGCP485 4th Meeting, Algiers, Algeria, 2 September 2006.
24. El Kabouri, J.; Triantafyllou, A.; Errami, E.; Belkacim, S.; Calassou, E.; Zouicha, A.; Linnemann, U. Revising the Lithostratigraphic Framework of the Ediacaran Succession of the Anti-Atlas Belt: Correlation across the Cadomian Domain of the West African Craton. *J. Afr. Earth Sci.* **2025**, *229*, 105696. [CrossRef]
25. Errami, E.; Linnemann, U.; Hofmann, M.; Gärtner, A.; Zieger, J.; Gärtner, J.; Mende, K.; El Kabouri, J.; Gasquet, D.; Ennih, N. From Pan-African Transpression to Cadomian Transtension at the West African Margin: New U–Pb Zircon Ages from the Eastern Saghro Inlier (Anti-Atlas, Morocco). *SP* **2021**, *503*, 209–233. [CrossRef]
26. Ouguir, H. Cadre Structural Du Gîte Ag-Hg d'Imiter (Anti-Atlas, Maroc); Implication Métallogénique. *Bull. De La. Société Géologique De Fr.* **1994**, *165*, 233–248.
27. Ouguir, H.; Macaudiere, J.; Dagallier, G. Le protérozoïque supérieur d'imiter, Saghro oriental, Maroc: Un contexte géodynamique d'arrière-arc. *J. Afr. Earth Sci.* **1996**, *22*, 173–189. [CrossRef]
28. Hefferan, K.; Soulaimani, A.; Samson, S.D.; Admou, H.; Inglis, J.; Saquaque, A.; Latifa, C.; Heywood, N. A Reconsideration of Pan African Orogenic Cycle in the Anti-Atlas Mountains, Morocco. *J. Afr. Earth Sci.* **2014**, *98*, 34–46. [CrossRef]
29. Choubert, G. L'accident Majeur de l'Anti-Atlas. *Comptes Rendus De l'Académie Des Sci. Paris* **1947**, *224*, 1172–1173.
30. Blein, O.; Chevremont, P.; Baudin, T.; Hafid, A.; Admou, H.; Soulaimani, A.; Ouanaimi, H.; Bouabdelli, M.; Gasquet, D.; Padel, M. Contrasting Paleoproterozoic Granitoids in the Kerdous, Tagragra d'Akka, Agadir-Melloul and Iguerda Inliers (Western Anti-Atlas, Morocco). *J. Afr. Earth Sci.* **2022**, *189*, 104500. [CrossRef]
31. Blein, O.; Baudin, T.; Chèvremont, P.; Soulaimani, A.; Admou, H.; Gasquet, P.; Cocherie, A.; Egal, E.; Youbi, N.; Razin, P.; et al. Geochronological Constraints on the Polycyclic Magmatism in the Bou Azzer-El Graara Inlier (Central Anti-Atlas Morocco). *J. Afr. Earth Sci.* **2014a**, *99*, 287–306. [CrossRef]
32. Gasquet, D.; Ennih, N.; Liégeois, J.-P.; Soulaimani, A.; Michard, A. The Pan-African Belt. In *Continental Evolution: The Geology of Morocco*; Michard, A., Saddiqi, O., Chalouan, A., Lamotte, D.F.D., Eds.; Lecture Notes in Earth Sciences; Springer: Berlin, Heidelberg, 2008; Volume 116, pp. 33–64. ISBN 978-3-540-77075-6.
33. Walsh, G.J.; Aleinikoff, J.N.; Benziane, F.; Yazidi, A.; Armstrong, T.R. U–Pb Zircon Geochronology of the Paleoproterozoic Tagragra de Tata Inlier and Its Neoproterozoic Cover, Western Anti-Atlas, Morocco. *Precambrian Res.* **2002**, *117*, 1–20. [CrossRef]
34. Ikenne, M.; Souhassou, M.; Arai, S. Introduction to Geodynamics of North Africa. *J. Afr. Earth Sci.* **2017**, *127*, 1–2. [CrossRef]
35. Ait Lahna, A.; Youbi, N.; Tassinari, C.C.G.; Basei, M.A.S.; Ernst, R.E.; Chaib, L.; Barzouk, A.; Mata, J.; Gärtner, A.; Admou, H.; et al. Revised Stratigraphic Framework for the Lower Anti-Atlas Supergroup Based on U–Pb Geochronology of Magmatic and Detrital Zircons (Zenaga and Bou Azzer-El Graara Inliers, Anti-Atlas Belt, Morocco). *J. Afr. Earth Sci.* **2020**, *171*, 103946. [CrossRef]
36. Michard, A.; Gasquet, D. Comment on "U–Pb Baddeleyite Ages and Geochemistry of Dolerite Dykes in the Bas Drâa Inlier of the Anti-Atlas of Morocco: Newly Identified 1380Ma Event in the West African Craton" by El Bahat et Al. *Lithos* **2013**, *174*, 99–100. [CrossRef]

37. Bouougri, E.H.; Lahna, A.A.; Tassinari, C.C.G.; Basei, M.A.S.; Youbi, N.; Admou, H.; Saquaque, A.; Boumehdi, M.A.; Maacha, L. Time Constraints on Early Tonian Rifting and Cryogenian Arc Terrane-Continent Convergence along the Northern Margin of the West African Craton: Insights from SHRIMP and LA-ICP-MS Zircon Geochronology in the Pan-African Anti-Atlas Belt (Morocco). *Gondwana Res.* **2020**, *85*, 169–188. [CrossRef]
38. Ikenne, M.; Souhassou, M.; Saintilan, N.J.; Karfal, A.; Hassani, A.E.L.; Moundi, Y.; Ousbih, M.; Ezzghoudi, M.; Zouhir, M.; Maacha, L. Cobalt–Nickel–Copper Arsenide, Sulfarsenide and Sulfide Mineralization in the Bou Azzer Window, Anti-Atlas, Morocco: One Century of Multi-Disciplinary and Geological Investigations, Mineral Exploration and Mining. *SP* **2021**, *502*, 45–66. [CrossRef]
39. Leblanc, M.; Lancelot, J.R. Interprétation Géodynamique Du Domaine Pan-Africain (Précambrien Terminal) de l'Anti-Atlas (Maroc) à Partir de Données Géologiques et Géochronologiques. *Can. J. Earth Sci.* **1980**, *17*, 142–155. [CrossRef]
40. Hodel, F.; Triantafyllou, A.; Berger, J.; Macouin, M.; Baele, J.-M.; Mattielli, N.; Monnier, C.; Trindade, R.I.F.; Ducea, M.N.; Chatir, A.; et al. The Moroccan Anti-Atlas Ophiolites: Timing and Melting Processes in an Intra-Oceanic Arc-Back-Arc Environment. *Gondwana Res.* **2020**, *86*, 182–202. [CrossRef]
41. Chaib, L.; Ait Lahna, A.; Admou, H.; Youbi, N.; El Moume, W.; Tassinari, C.C.G.; Mata, J.; Basei, M.A.S.; Sato, K.; Marzoli, A.; et al. Geochemistry and Geochronology of the Neoproterozoic Backarc Basin Khzama Ophiolite (Anti-Atlas Mountains, Morocco): Tectonomagmatic Implications. *Minerals* **2021**, *11*, 56. [CrossRef]
42. Michard, A.; Soulaimani, A.; Ouanaimi, H.; Raddi, Y.; Aït Brahim, L.; Rjimati, E.-C.; Baidder, L.; Saddiqi, O. Saghro Group in the Ougnat Massif (Morocco), an Evidence for a Continuous Cadomian Basin along the Northern West African Craton. *Comptes Rendus. Géoscience* **2017**, *349*, 81–90. [CrossRef]
43. Walsh, G.J.; Benziane, F.; Aleinikoff, J.N.; Harrison, R.W.; Yazidi, A.; Burton, W.C.; Quick, J.E.; Saadane, A. Neoproterozoic Tectonic Evolution of the Jebel Saghro and Bou Azzer—El Graara Inliers, Eastern and Central Anti-Atlas, Morocco. *Precambrian Res.* **2012**, *216–219*, 23–62. [CrossRef]
44. Youbi, N.; Ernst, R.E.; Söderlund, U.; Boumehdi, M.A.; Lahna, A.A.; Tassinari, C.C.G.; Moume, W.E.; Bensalah, M.K. The Central Iapetus Magmatic Province: An Updated Review and Link with the ca. 580 Ma Gaskiers Glaciation. In *Mass Extinctions, Volcanism, and Impacts: New Developments*; Adatte, T., Bond, D.P.G., Keller, G., Eds.; Geological Society of America: Boulder, CO, USA, 2020; pp. 35–66. ISBN 978-0-8137-2544-4.
45. Oukhro, R.; Youbi, N.; Kalderon-Asael, B.; Evans, D.A.D.; Pierce, J.; Wotzlaw, J.-F.; Ovtcharova, M.; Mata, J.; Mediany, M.A.; Ounar, J.; et al. Volcanic Stratigraphy, Petrology, Geochemistry and Precise U-Pb Zircon Geochronology of the Late Ediacaran Ouarzazate Group at the Oued Dar'a Caldera: Intracontinental Felsic Super-Eruptions in Association with Continental Flood Basalt Magmatism on the West African Craton (Saghro Massif, Anti-Atlas). *Minerals* **2025**, *15*, 776. [CrossRef]
46. Mediany, M.A.; Youbi, N.; Ben Chra, M.; Moutbir, O.; Hadimi, I.; Mata, J.; Wotzlaw, J.-F.; Madeira, J.; Doblas, M.; Khalaf, E.E.D.A.H.; et al. Volcanic Response to Post-Pan-African Orogeny Delamination: Insights from Volcanology, Precise U-Pb Geochronology, Geochemistry, and Petrology of the Ediacaran Ouarzazate Group of the Anti-Atlas, Morocco. *Minerals* **2025**, *15*, 142. [CrossRef]
47. Soulaimani, A.; Burkhard, M. The Anti-Atlas Chain (Morocco): The Southern Margin of the Variscan Belt along the Edge of the West African Craton. *SP* **2008**, *297*, 433–452. [CrossRef]
48. Atif, Y.; Soulaimani, A.; Ait Lahna, A.; Yaagoub, D.; Youbi, N.; Pour, A.B.; Hashim, M. Structural Analysis and Paleostress Evolution in the Imiter Silver Mining Region, Eastern Anti Atlas, Morocco: Implications for Mineral Exploration. *Minerals* **2022**, *12*, 1563. [CrossRef]
49. Baidada, B.; Ikenne, M.; Barbey, P.; Soulaimani, A.; Cousens, B.; Haissen, F.; Ilmen, S.; Alansari, A. SHRIMP U–Pb Zircon Geochronology of the Granitoids of the Imiter Inlier: Constraints on the Pan-African Events in the Saghro Massif, Anti-Atlas (Morocco). *J. Afr. Earth Sci.* **2019**, *150*, 799–810. [CrossRef]
50. Gerd Geyer, E.L. *Ediacaran–Cambrian Depositional Environments and Stratigraphy of the Western Atlas Regions*; Infracambrian/Early Palaeozoic Field Guide Series No. 1; UCL Maghreb Petroleum Research Group (MPRG): London, UK, 2006.
51. Geyer, G.; Landing, E. Cambrian Deposition in Northwestern Africa: Relationship of Tamlelt Massif (Moroccan-Algerian Border Region) Succession to the Moroccan Meseta. *J. Afr. Earth Sci.* **2020**, *165*, 103772. [CrossRef]
52. Schiavo, A.; Taj-Eddine, K.; Algouti, A.; Benvenuti, M.; Dal Piaz, G.V.; Eddebbi, A.; El Boukhari, A.; Laftouhi, N.; Massironi, M.; Moratti, G. *Carte Géologique du Maroc au 1/50,000, Feuille Imtir—Notice Explicative*; Notes et Mémoires du Service Géologique du Maroc, No. 518 bis; Service de la Carte Géologique du Maroc: Rabat, Morocco, 2007.
53. Grappe, J. L'ancien Gisement d'argent d'Imiter (Djebel Sarhro, Maroc). Ph.D. Thesis, Université Claude Bernard, Lyon, France, 1976.
54. Cheilletz, A.; Levresse, G.; Gasquet, D.; Azizi-Samir, M.; Zyadi, R.; Archibald, D.A.; Farrar, E. The Giant Imiter Silver Deposit: Neoproterozoic Epithermal Mineralization in the Anti-Atlas, Morocco. *Min. Depos.* **2002**, *37*, 772–781. [CrossRef]
55. Hindermeyer, J. *Carte Géologique de l'Anti-Atlas Oriental: Feuille Dadès et Jbel Saghro: Notes et Mémoires Du Service Géologique Du Maroc*; Service Géologique du Maroc: Rabat, Morocco, 1977.

56. Tuduri, J.; Chauvet, A.; Barbanson, L.; Bourdier, J.-L.; Labriki, M.; Ennaciri, A.; Badra, L.; Dubois, M.; Ennaciri-Leloix, C.; Sizaret, S.; et al. The Jbel Saghro Au(–Ag, Cu) and Ag–Hg Metallogenetic Province: Product of a Long-Lived Ediacaran Tectono-Magmatic Evolution in the Moroccan Anti-Atlas. *Minerals* **2018b**, *8*, 592. [CrossRef]
57. Guillou, C. Repeatability and Reproducibility of Site-Specific Isotope Ratios in Quantitative ^{2}H-NMR. *Magn. Reson. Chem.* **1988**, *26*, 491. [CrossRef]
58. Hejja, Y.; Bourdier, J.-L.; Gaouzi, A.; Baidder, L.; Tuduri, J.; Ennaciri, A.; Zakir, A.; Maacha, L.; Zouhair, M. Lithostratigraphy and Structural Framework of the Ediacaran Volcano-Plutonic Complex of the Imiter Ag–Hg Mining District (Jbel Saghro, Anti-Atlas, Morocco). *J. Afr. Earth Sci.* **2022**, *196*, 104687. [CrossRef]
59. Tuduri, J.; Chauvet, A.; Ennaciri, A.; Barbanson, L. Modèle de Formation Du Gisement d'argent d'Imiter (Anti-Atlas Oriental, Maroc). Nouveaux Apports de l'analyse Structurale et Minéralogique. *Comptes Rendus. Géoscience* **2006**, *338*, 253–261. [CrossRef]
60. Baidada, B.; Cousens, B.; Alansari, A.; Soulaimani, A.; Barbey, P.; Ilmen, S.; Ikenne, M. Geochemistry and Sm–Nd Isotopic Composition of the Imiter Pan-African Granitoids (Saghro Massif, Eastern Anti-Atlas, Morocco): Geotectonic Implications. *J. Afr. Earth Sci.* **2017**, *127*, 99–112. [CrossRef]
61. De Wall, H. Âge de Mise En Place et Contexte Géologique Des Granitoïdes de La Boutonnière d'Imiter (Saghro Oriental, Anti-Atlas, Maroc) . In Proceedings of the 2ème Colloque International 3MA (Magmatisme, Métamorphisme & Minéralisations Associées), Marrakech, Morroco, 10–12 May 2001; p. 19.
62. Gasquet, D.; Levresse, G.; Cheilletz, A.; Azizi-Samir, M.R.; Mouttaqi, A. Contribution to a Geodynamic Reconstruction of the Anti-Atlas (Morocco) during Pan-African Times with the Emphasis on Inversion Tectonics and Metallogenic Activity at the Precambrian–Cambrian Transition. *Precambrian Res.* **2005**, *140*, 157–182. [CrossRef]
63. Yajioui, Z.; Karaoui, B.; Chew, D.; Breitkreuz, C.; Mahmoudi, A. U–Pb Zircon Geochronology of the Ediacaran Volcano-Sedimentary Succession of the NE Saghro Inlier (Anti-Atlas, Morocco): Chronostratigraphic Correlation on the Northwestern Margin of Gondwana. *Gondwana Res.* **2020**, *87*, 263–277. [CrossRef]
64. Ousbih, M.; Ikenne, M.; Cousens, B.; Chelle-Michou, C.; El Bilali, H.; Gaouzi, A.; Markovic, S.; Askkour, F.; Mouhajir, M.; El Mouden, S.; et al. Stratigraphy, Geochronology, Geochemistry and Nd Isotopes of the Ouarzazate Group, Anti-Atlas, Morocco: Evidence of a Late Neoproterozoic LIP in the Northwestern Part of the West African Craton. *Lithos* **2024**, *474–475*, 107593. [CrossRef]
65. Raczek, I.; Stoll, B.; Hofmann, A.W.; Peter Jochum, K. High-Precision Trace Element Data for the USGS Reference Materials BCR-1, BCR-2, BHVO-1, BHVO-2, AGV-1, AGV-2, DTS-1, DTS-2, GSP-1 and GSP-2 by ID-TIMS and MIC-SSMS. *Geostand. Newsl.* **2001**, *25*, 77–86. [CrossRef]
66. Jochum, K.P.; Weis, U.; Schwager, B.; Stoll, B.; Wilson, S.A.; Haug, G.H.; Andreae, M.O.; Enzweiler, J. Reference Values Following ISO Guidelines for Frequently Requested Rock Reference Materials. *Geostand. Geoanalytic Res.* **2016**, *40*, 333–350. [CrossRef]
67. Richard, P.; Shimizu, N.; Allègre, C.J. 143Nd/146Nd, a Natural Tracer: An Application to Oceanic Basalts. *Earth Planet. Sci. Lett.* **1976**, *31*, 269–278. [CrossRef]
68. Garçon, M.; Boyet, M.; Carlson, R.W.; Horan, M.F.; Auclair, D.; Mock, T.D. Factors Influencing the Precision and Accuracy of Nd Isotope Measurements by Thermal Ionization Mass Spectrometry. *Chem. Geol.* **2018**, *476*, 493–514. [CrossRef]
69. Weis, D.; Kieffer, B.; Maerschalk, C.; Barling, J.; De Jong, J.; Williams, G.A.; Hanano, D.; Pretorius, W.; Mattielli, N.; Scoates, J.S.; et al. High-precision Isotopic Characterization of USGS Reference Materials by TIMS and MC-ICP-MS. *Geochem Geophys Geosyst* **2006**, *7*, 2006GC001283. [CrossRef]
70. Bouvier, A.; Vervoort, J.D.; Patchett, P.J. The Lu–Hf and Sm–Nd Isotopic Composition of CHUR: Constraints from Unequilibrated Chondrites and Implications for the Bulk Composition of Terrestrial Planets. *Earth Planet. Sci. Lett.* **2008**, *273*, 48–57. [CrossRef]
71. Faure, G. G. Faure 1986. Principles of Isotope Geology, 2nd Ed. Xv + 589 Pp. New York, Chichester, Brisbane, Toronto, Singapore: John Wiley & Sons. Price £41.30 (Hard Covers), ISBN 0 471 86412 9 (Hard Covers). £17.20, US $25.90 (Paperback). *Geol. Mag.* **1987**, *124*, 594–595. [CrossRef]
72. Coplen, T.B.; Brand, W.A.; Gehre, M.; Gröning, M.; Meijer, H.A.J.; Toman, B.; Verkouteren, R.M. New Guidelines for δ^{13} C Measurements. *Anal. Chem.* **2006**, *78*, 2439–2441. [CrossRef] [PubMed]
73. Higginson, M.J. Geochemical Proxies (Non-Isotopic). In *Encyclopedia of Paleoclimatology and Ancient Environments*; Encyclopedia of Earth Sciences Series; Gornitz, V., Ed.; Springer: Dordrecht, The Netherlands, 2009; pp. 341–354. ISBN 978-1-4020-4551-6.
74. Hayashi, K.-I.; Fujisawa, H.; Holland, H.D.; Ohmoto, H. Geochemistry of ~1.9 Ga Sedimentary Rocks from Northeastern Labrador, Canada. *Geochim. Et. Cosmochim. Acta* **1997**, *61*, 4115–4137. [CrossRef] [PubMed]
75. Cox, R.; Lowe, D.R.; Cullers, R.L. The Influence of Sediment Recycling and Basement Composition on Evolution of Mudrock Chemistry in the Southwestern United States. *Geochim. Et. Cosmochim. Acta* **1995**, *59*, 2919–2940. [CrossRef]
76. Fedo, C.M.; Wayne Nesbitt, H.; Young, G.M. Unraveling the Effects of Potassium Metasomatism in Sedimentary Rocks and Paleosols, with Implications for Paleoweathering Conditions and Provenance. *Geol* **1995**, *23*, 921. [CrossRef]
77. Harnois, L. The CIW Index: A New Chemical Index of Weathering. *Sediment. Geol.* **1988**, *55*, 319–322. [CrossRef]

78. Algeo, T.J.; Maynard, J.B. Trace-Element Behavior and Redox Facies in Core Shales of Upper Pennsylvanian Kansas-Type Cyclothems. *Chem. Geol.* **2004**, *206*, 289–318. [CrossRef]
79. Tribovillard, N.; Algeo, T.J.; Lyons, T.; Riboulleau, A. Trace Metals as Paleoredox and Paleoproductivity Proxies: An Update. *Chem. Geol.* **2006**, *232*, 12–32. [CrossRef]
80. Galarraga, F.; Reategui, K.; Martïnez, A.; Martínez, M.; Llamas, J.F.; Márquez, G. V/Ni Ratio as a Parameter in Palaeoenvironmental Characterisation of Nonmature Medium-Crude Oils from Several Latin American Basins. *J. Pet. Sci. Eng.* **2008**, *61*, 9–14. [CrossRef]
81. Zhou, C.; Jiang, S.-Y. Palaeoceanographic Redox Environments for the Lower Cambrian Hetang Formation in South China: Evidence from Pyrite Framboids, Redox Sensitive Trace Elements, and Sponge Biota Occurrence. *Palaeogeogr. Palaeoclimatol. Palaeoecol.* **2009**, *271*, 279–286. [CrossRef]
82. Akinlua, A.; Maende, A.; Adekola, S.A.; Swakamisa, O.; Fadipe, O.A.; Akinyemi, S.A. Source Rock Potential of Selected Cretaceous Shales, Orange Basin, South Africa. *Int. Geol. Rev.* **2011**, *53*, 1508–1521. [CrossRef]
83. Pi, D.-H.; Jiang, S.-Y.; Luo, L.; Yang, J.-H.; Ling, H.-F. Depositional Environments for Stratiform Witherite Deposits in the Lower Cambrian Black Shale Sequence of the Yangtze Platform, Southern Qinling Region, SW China: Evidence from Redox-Sensitive Trace Element Geochemistry. *Palaeogeogr. Palaeoclimatol. Palaeoecol.* **2014**, *398*, 125–131. [CrossRef]
84. Whitney, D.L.; Evans, B.W. Abbreviations for Names of Rock-Forming Minerals. *Am. Mineral.* **2010**, *95*, 185–187. [CrossRef]
85. Kramer, W.; Weatherall, G.; Offler, R. Origin and Correlation of Tuffs in the Permian Newcastle and Wollombi Coal Measures, NSW, Australia, Using Chemical Fingerprinting. *Int. J. Coal Geol.* **2001**, *47*, 115–135. [CrossRef]
86. Moosavirad, S.M.; Janardhana, M.R.; Sethumadhav, M.S.; Moghadam, M.R.; Shankara, M. Geochemistry of Lower Jurassic Shales of the Shemshak Formation, Kerman Province, Central Iran: Provenance, Source Weathering and Tectonic Setting. *Geochemistry* **2011**, *71*, 279–288. [CrossRef]
87. Dai, S.; Li, T.; Jiang, Y.; Ward, C.R.; Hower, J.C.; Sun, J.; Liu, J.; Song, H.; Wei, J.; Li, Q.; et al. Mineralogical and Geochemical Compositions of the Pennsylvanian Coal in the Hailiushu Mine, Daqingshan Coalfield, Inner Mongolia, China: Implications of Sediment-Source Region and Acid Hydrothermal Solutions. *Int. J. Coal Geol.* **2015**, *137*, 92–110. [CrossRef]
88. Armstrong-Altrin, J.S. Provenance of Sands from Cazones, Acapulco, and Bahía Kino Beaches, México. *Rev. Mex. Cienc. Geológicas* **2009**, *26*, 764–782.
89. Bas, M.J.L.; Maitre, R.W.L.; Streckeisen, A.; Zanettin, B. IUGS Subcommission on the Systematics of Igneous Rocks A Chemical Classification of Volcanic Rocks Based on the Total Alkali-Silica Diagram. *J. Petrol.* **1986**, *27*, 745–750. [CrossRef]
90. McLennan, S.M.; Nance, W.B.; Taylor, S.R. Rare Earth Element-Thorium Correlations in Sedimentary Rocks, and the Composition of the Continental Crust. *Geochim. Et. Cosmochim. Acta* **1980**, *44*, 1833–1839. [CrossRef]
91. Schieber, J. A Combined Petrographical—Geochemical Provenance Study of the Newland Formation, Mid-Proterozoic of Montana. *Geol. Mag.* **1992**, *129*, 223–237. [CrossRef]
92. Grevenitz, P.; Carr, P.; Hutton, A. Origin, Alteration and Geochemical Correlation of Late Permian Airfall Tuffs in Coal Measures, Sydney Basin, Australia. *Int. J. Coal Geol.* **2003**, *55*, 27–46. [CrossRef]
93. Zhang, Y.; Liao, Z.; Chen, A.; Cao, J.; Zhang, B.; Wei, Y.; Shi, Q. Extreme Organic Matter Enrichment in the Ediacaran Doushantuo Formation: New Constraints from the NE Sichuan Basin, China. *Mar. Pet. Geol.* **2024**, *165*, 106866. [CrossRef]
94. Liu, H.; Wang, C.; Li, Y.; Deng, J.; Deng, B.; Feng, Y.; Chen, H.; Xu, Y.; Zhao, S. Geochemistry of the Black Rock Series of Lower Cambrian Qiongzhusi Formation, SW Yangtze Block, China: Reconstruction of Sedimentary and Tectonic Environments. *Open Geosci.* **2021**, *13*, 166–187. [CrossRef]
95. Floyd, P.A.; Leveridge, B.E. Tectonic Environment of the Devonian Gramscatho Basin, South Cornwall: Framework Mode and Geochemical Evidence from Turbiditic Sandstones. *JGS* **1987**, *144*, 531–542. [CrossRef]
96. Bankole, O.M.; El Albani, A.; Meunier, A.; Poujol, M.; Bekker, A. Elemental Geochemistry and Nd Isotope Constraints on the Provenance of the Basal Siliciclastic Succession of the Middle Paleoproterozoic Francevillian Group, Gabon. *Precambrian Res.* **2020**, *348*, 105874. [CrossRef]
97. Jahn, B.-M.; Condie, K.C. Evolution of the Kaapvaal Craton as Viewed from Geochemical and Sm-Nd Isotopic Analyses of Intracratonic Pelites. *Geochim. Et. Cosmochim. Acta* **1995**, *59*, 2239–2258. [CrossRef]
98. Nelson, B.K.; DePAOLO, D.J. Rapid Production of Continental Crust 1.7 to 1.9 b.y. Ago: Nd Isotopic Evidence from the Basement of the North American Mid-Continent. *Geol. Soc. Am. Bull.* **1985**, *96*, 746. [CrossRef]
99. Barbey, P.; Nachit, H.; Pons, J. Magma–Host Interactions during Differentiation and Emplacement of a Shallow-Level, Zoned Granitic Pluton (Tarçouate Pluton, Morocco): Implications for Magma Emplacement. *Lithos* **2001**, *58*, 125–143. [CrossRef]
100. Ennih, N.; Liégeois, J.-P. The Boundaries of the West African Craton, with Special Reference to the Basement of the Moroccan Metacratonic Anti-Atlas Belt. *Spec. Publ.* **2008**, *297*, 1–17. [CrossRef]

101. Askkour, F.; Ikenne, M.; Chelle-Michou, C.; Cousens, B.L.; Markovic, S.; Ousbih, M.; Souhassou, M.; El Bilali, H.; Ernst, R. Geochronology and Petrogenesis of Granitoids from the Bas Draa Inlier (Western Anti-Atlas, Morocco): Revived Debate on the Tectonic Regime Operating during Early Paleoproterozoic at the NW Edge of the West African Craton. *Geochemistry* **2024**, *84*, 126044. [CrossRef]
102. Triantafyllou, A.; Berger, J.; Baele, J.-M.; Bruguier, O.; Diot, H.; Ennih, N.; Monnier, C.; Plissart, G.; Vandycke, S.; Watlet, A. Intra-Oceanic Arc Growth Driven by Magmatic and Tectonic Processes Recorded in the Neoproterozoic Bougmane Arc Complex (Anti-Atlas, Morocco). *Precambrian Res.* **2018**, *304*, 39–63. [CrossRef]
103. Lécolle, M.; Derré, C.; Nerci, K. The Proterozoic Sulphide Alteration Pipe of Sidi Flah and Its Host Series. New Data for the Geotectonic Evolution of the Pan-African Belt in the Eastern Anti-Atlas (Morocco). *Ore Geol. Rev.* **1991**, *6*, 501–536. [CrossRef]
104. Fekkak, A.; Boualoul, M.; Badra, L.; Amenzou, M.; Saquaque, A.; El-Amrani, I.E. Origine et contexte geotectonique des depots detritiques du groupe neoproterozoïque inferieur de Kelaat Mgouna (Anti-Atlas Oriental, Maroc). *J. Afr. Earth Sci.* **2000**, *30*, 295–311. [CrossRef]
105. Roser, B.P.; Korsch, R.J. Determination of Tectonic Setting of Sandstone-Mudstone Suites Using SiO_2 Content and K_2O/Na_2O Ratio. *J. Geol.* **1986**, *94*, 635–650. [CrossRef]
106. Fekkak, A.; Pouclet, A.; Benharref, M. The Middle Neoproterozoic Sidi Flah Group (Anti-Atlas, Morocco): Synrift Deposition in a Pan-African Continent/Ocean Transition Zone. *J. Afr. Earth Sci.* **2003**, *37*, 73–87. [CrossRef]
107. Pettijohn, F.J.; Potter, P.E.; Siever, R. *Sand and Sandstone*; Springer: New York, NY, USA, 1987; ISBN 978-0-387-96350-1.
108. Suttner, L.J.; Dutta, P.K. Dutta Alluvial Sandstone Composition and Paleoclimate, I. Framework Mineralogy. *SEPM JSR* **1986**, *Vol. 56*. [CrossRef]
109. Dhannoun, H.Y.; Al-Dlemi, A.M.S. The Relation between Li, V, P2O5, and Al2O3 Contents in Marls and Mudstones as Indicators of Environment of Deposition. *Arab J. Geosci.* **2013**, *6*, 817–823. [CrossRef]
110. Arthur, M.A.; Sageman, B.B. MARINE BLACK SHALES: Depositional Mechanisms and Environments of Ancient Deposits. *Annu. Rev. Earth Planet. Sci.* **1994**, *22*, 499–551. [CrossRef]
111. Tyson, R.V. *Sedimentary Organic Matter*; Springer: Dordrecht, The Netherlands, 1995; ISBN 978-94-010-4318-2.
112. Fike, D.A.; Grotzinger, J.P.; Pratt, L.M.; Summons, R.E. Oxidation of the Ediacaran Ocean. *Nature* **2006**, *444*, 744–747. [CrossRef] [PubMed]
113. McFadden, K.A.; Huang, J.; Chu, X.; Jiang, G.; Kaufman, A.J.; Zhou, C.; Yuan, X.; Xiao, S. Pulsed Oxidation and Biological Evolution in the Ediacaran Doushantuo Formation. *Proc. Natl. Acad. Sci. USA* **2008**, *105*, 3197–3202. [CrossRef] [PubMed]
114. Cui, H.; Kaufman, A.J.; Xiao, S.; Peek, S.; Cao, H.; Min, X.; Cai, Y.; Siegel, Z.; Liu, X.-M.; Peng, Y.; et al. Environmental Context for the Terminal Ediacaran Biomineralization of Animals. *Geobiology* **2016**, *14*, 344–363. [CrossRef] [PubMed]
115. Knoll, A.H.; Walter, M.R.; Narbonne, G.M.; Christie-Blick, N. The Ediacaran Period: A New Addition to the Geologic Time Scale. *LET* **2006**, *39*, 13–30. [CrossRef]
116. Gao, Y.; Zhang, X.; Xu, Y.; Fang, C.; Gong, Y.; Shen, Y. High Primary Productivity during the Ediacaran Period Revealed by the Covariation of Paired C-Isotopic Records from South China. *Precambrian Res.* **2020**, *349*, 105411. [CrossRef]

Disclaimer/Publisher's Note: The statements, opinions and data contained in all publications are solely those of the individual author(s) and contributor(s) and not of MDPI and/or the editor(s). MDPI and/or the editor(s) disclaim responsibility for any injury to people or property resulting from any ideas, methods, instructions or products referred to in the content.